A Melting Layer Model for Passive/Active Microwave Remote Sensing Applications- Part I: Model Formulation and Comparison with Observations

William S. Olson[1], Peter Bauer[2], Nicolas F. Viltard[3], Daniel E. Johnson[4],
and Wei-Kuo Tao[5]

[1]JCET, University of Maryland Baltimore County

[2]Deutsche Forschungsanstalt fuer Luft- und Raumfahrt

[3]Centre détudes des Environnements Terrestre et Planétaires

[4]Science Systems and Applications, Inc.

[5]Laboratory for Atmospheres, NASA/Goddard Space Flight Center

to be submitted to the *Journal of Applied Meteorology*

January 4, 2000

Abstract

In this study, a 1-D steady-state microphysical model which describes the vertical distribution of melting precipitation particles is developed. The model is driven by the ice-phase precipitation distributions just above the freezing level at applicable gridpoints of "parent" 3-D cloud-resolving model (CRM) simulations. It extends these simulations by providing the number density and meltwater fraction of each particle in finely-separated size categories through the melting layer. The depth of the modeled melting layer is primarily determined by the initial material density of the ice-phase precipitation.

The radiative properties of melting precipitation at microwave frequencies are calculated based upon different methods for describing the dielectric properties of mixed-phase particles. Particle absorption and scattering efficiencies at the Tropical Rainfall Measuring Mission Microwave Imager frequencies (10.65 to 85.5 GHz) are enhanced greatly for relatively small (~0.1) meltwater fractions. The relatively large number of partially-melted particles just below the freezing level in stratiform regions leads to significant microwave absorption, well-exceeding the absorption by rain at the base of the melting layer. Calculated precipitation backscatter efficiencies at the Precipitation Radar frequency (13.8 GHz) increase in proportion to the particle meltwater fraction, leading to a "bright-band" of enhanced radar reflectivities in agreement with previous studies.

The radiative properties of the melting layer are determined by the choice of dielectric models and the initial water contents and material densities of the “seeding” ice-phase precipitation particles. Simulated melting layer profiles based upon snow described by the Fabry-Szyrmer core-shell dielectric model and graupel described by the Maxwell-Garnett water matrix dielectric model lead to reasonable agreement with radar-derived melting layer optical depth distributions. Moreover, control profiles that do not contain mixed-phase precipitation particles yield optical depths that are systematically lower than those observed. Therefore, the use of the melting layer model to extend 3-D CRM simulations appears justified, at least until more realistic spectral methods for describing melting precipitation in high-resolution, 3-D CRM’s are implemented.

1. Introduction

Several methods for estimating instantaneous precipitation rates from spaceborne passive microwave radiometer measurements have been developed and applied with moderate success; Smith et al. (1994). In recent years, these rainfall retrieval methods have been primarily applied to observations of the Special Sensor Microwave/Imager (SSM/I), a component of several of the Defense Meteorological Satellite Program's polar-orbiting platforms. Intercomparisons of the methods have demonstrated the utility of physically-based rainfall algorithms, which rely on physical models relating the three-dimensional structure of precipitating clouds to the upwelling radiances measured by the SSM/I; ref. Ebert and Manton (1998). The launch of the Tropical Rainfall Measuring Mission (TRMM) Microwave Imager (TMI) in November, 1997, improved upon the capability of SSM/I by extending the channel frequency range (10.65 - 85.5 GHz) and resolution (5 km minimum footprint). In addition, a 13.8 GHz weather radar called the Precipitation Radar (PR) was included on the TRMM platform to provide detailed vertical structure (250 m resolution) of the observed precipitation.

By extending the passive radiometer physical models to include a description of the radar response to precipitation, retrieval procedures combining both radiometer and radar observations are achieved. Such physically based methods have already been developed and applied to TMI and PR data; e.g. Haddad, et al. (1997). However, the physical models supporting these retrieval methods do not include an explicit representation of melting precipitation particles, which have an important radiative effect in stratiform rain regions.

Previous studies by Schols et al. (1997), Meneghini and Liou (1996, 1997), and Bauer et al. (1999a), have indicated the possibility of significant absorption of microwaves by partially-melted particles, in addition to the commonly-observed enhanced radar reflectivity of the melting layer. Although the high radar reflectivities of melting hydrometeors typically occupy only a thin layer (~500 m), and thus might be ignored, the microwave absorption within the melting layer has more serious consequences for both radiometric and radar remote sensing of stratiform precipitation. Absorption and emission of microwaves by the melting layer might account for a significant portion of the emission observed by spaceborne passive radiometers- emission that might otherwise be attributed to liquid precipitation in physically-based retrieval methods. Likewise, the 2-way path attenuation of radar pulses by the melting layer must be included in calculations of the total attenuation of reflectivities measured by spaceborne radar.

In the present study, a one-dimensional, steady-state microphysical model of melting ice hydrometeors is developed, following the work of Bauer et al. (1999b). Although simplified, the model yields the volume fractions of ice, air, and water of melting particles of all species and sizes at a fine grid spacing in the vertical. This model is used in the manner of a parameterization to describe the vertical distribution of melting precipitation at applicable horizontal gridpoints of fully three-dimensional cloud resolving model simulations.

The extinction optical depth and reflectivity simulations are compared to the corresponding PR-derived quantities in an attempt to determine which modeling assumptions lead to simulations most consistent with the observations.

2. Model Description

a. Microphysics of the Melting Model

Calculation of the electromagnetic properties of melting layer requires, at the very least, a specification of the volume fractions of ice, air, and liquid of each melting particle within the ensemble of particles which comprise the layer. From these volume fractions, the dielectric properties of the particles may be computed according to different approximate formulae; see section 1c. In addition, accurate simulations of upwelling radiances from cloud and precipitation distributions require that these distributions be specified in three dimensions at a resolution greater than 12 km in the horizontal, as indicated by Kummerow (1998). Such fields can be obtained from 3-D cloud resolving model (CRM) simulations; however, the microphysical schemes utilized in CRM's typically do not contain an explicit description of partially-melted precipitation particles; e.g. Lin et al. (1983), Rutledge and Hobbs (1983; 1984), due to the large computational requirements. Also, it will be shown in section 1c that the height-variation of melting particle dielectric properties is significant on scales ~50 m, which is usually a much finer resolution than that provided by many CRM's. Therefore, in the present study a one-dimensional melting layer model is developed to describe the melting process at applicable horizontal gridpoints of a "parent" 3-D CRM simulation.

The melting model described in this study is only applicable to regions where updrafts and downdrafts are relatively weak in the vicinity of the freezing level. Under these conditions precipitation will fall steadily through the air column and only melting, sublimation/deposition, evaporation/condensation, and aggregation of particles need be considered. Each gridpoint of the parent model domain is first examined to find the maximum magnitude of the vertical velocity in the layer between the freezing level and two kilometers below it. If the magnitude of the vertical velocity does not exceed 0.5 m s^{-1} in this layer, and if ice-phase precipitation exists just above the freezing level, then the 1-D melting model is applied to the gridpoint in question.

The formulation of the melting layer model follows the simplified approach of Bauer et al. (1999b). The temperature, relative humidity, vertical air motion, and hydrometeor fields at each qualified gridpoint from the parent 3-D CRM simulation are first interpolated to the 50 m resolution melting model vertical grid; see Fig. 1. The top of the melting model domain is assumed to coincide with the parent model grid-level at, or just above, the 0 C level, and the bottom of the model domain is set 3 km below this level.

The size distributions of precipitation species (rain, snow, graupel) in the melting model are represented by number densities, $n(i,z)$, at intervals of 0.1 mm diameter. The index i indicates the particle diameter interval, and z is the depth below the model top. A particle of a given size is characterized by its ice mass, $m_{ice}(i,z)$, liquid water mass, $m_{liq}(i,z)$, and volume of air, $V_{air}(i,z)$.

At the top of the melting model domain the particle size distributions and composition are inherited from the parent model, therefore

$$n(i,0) = n_{init}\left(D_{init_i}\right), \tag{1}$$

where $n_{init}(D_{init\ i})$ is the parent model particle number density at the top of the melting model domain, and $n(i_i,0)$ is the melting model number density for an initial particle diameter $D_{init\ i}$ and depth $z = 0$ below the model top. Initially, ice precipitation species are assumed to be spherical and dry mixtures of ice and air (no melt water or collected water); therefore, the mass of ice and liquid in a given particle are

$$m_{ice}(i,0) = \left\{ \begin{array}{ll} \rho_m\left(D_{init_i}\right)\dfrac{\pi D_{init_i}^{\ 3}}{6}, & \text{ice species} \\ 0, & \text{rain} \end{array} \right. \tag{2}$$

and

$$m_{liq}(i,0) = \begin{cases} 0, & \text{ice species} \\ \rho_{liq}\dfrac{\pi D_{init_i}^{\,3}}{6}, & \text{rain,} \end{cases} \tag{3}$$

where $\rho_m(D_{init\,i})$ is the initial ice particle material density, which may be a function of diameter, and ρ_{liq} is the density of water, 1.0 g cm^{-3}. The small mass of air in the particle is neglected, but the volume of air within the particle can be calculated from

$$V_{air}(i,0) = \begin{cases} \dfrac{\pi D_{init_i}^{\,3}}{6}\left[\dfrac{\rho_{ice} - \rho_m\left(D_{init_i}\right)}{\rho_{ice}}\right], & \text{ice species} \\ 0, & \text{rain} \end{cases} \tag{4}$$

where ρ_{ice} is the density of pure ice, 0.917 g cm^{-3}. A description of the evolution of the precipitation particles as they fall from level z to a new depth z-Δz follows. The diameter index i and level argument z have been omitted unless they are required for clarity.

A particle of a given diameter D is assumed to fall at a terminal velocity given by

$$w_T = -\left(\frac{4\rho_m g}{3\rho_a C_D}\right)^{1/2} D^{1/2} \tag{5}$$

where ρ_m is the material density of the particle,

$$\rho_m = \frac{m_{ice} + m_{liq}}{\frac{m_{ice}}{\rho_{ice}} + \frac{m_{liq}}{\rho_{liq}} + V_{air}}, \tag{6}$$

g is the acceleration of gravity, ρ_a is the density of air, and C_D is the particle drag coefficient. Since the parent model simulation may have different fallspeed formulations, the drag coefficient C_D is determined such that the total mass flux of a given ice (rain) species is equal to the mass flux of that species in the parent model at the top (bottom) of the melting model domain. The parameterization (5) for terminal velocity is used because the net particle density of an ice particle may change as the particle melts, and (5) accounts for the change in terminal velocity as a function of particle density. A completely melted ice particle assumes the drag coefficient of rain.

As the ice precipitation particle of a given diameter falls, the rate of increase of the mass of melt water contained in the particle is determined by

$$\frac{dm_{melt}}{dt} = \begin{cases} \left(F_{sens} - F_{evap}\right)/L_f\,, & T > 273.16\,\mathrm{K}; F_{sens} > F_{evap} \\ 0, & \text{otherwise.} \end{cases} \tag{7}$$

Here, F_{sens} is the rate of sensible heat transfer to the particle, F_{evap} is the rate of latent heat loss due to the evaporation of melt water, and L_f is the latent heat of fusion, 3.34 x 10^5 j kg^{-1}. Note that melting can only occur if the temperature of the particle environment exceeds 273.16 K and the rate of sensible heat transfer exceeds the rate of heat loss due to evaporation. Equation (2) follows the development of Ferrier (1994) but neglects collection terms that may also affect the particle heat balance. The sensible heat transfer rate is given by

$$F_{sens} = 2\pi D\, K(T-T_o)\beta, \tag{8}$$

where K is the thermal conductivity of the air, T is the air temperature, T_o is the assumed melting particle temperature, 273.16 K, and β is the ventilation factor,

$$\beta = 0.78+0.31 Sc^{1/3} Re^{1/2}. \tag{9}$$

Here, Sc is the Schmidt number, which is given by

$$S_c = \mu/(\rho_a \psi), \tag{10}$$

and the Reynolds number is given by

$$Re = -w_T D \rho_a / \mu, \tag{11}$$

where μ is the dynamic viscosity of air and ψ is the diffusivity of water vapor in air. The physical parameters K, μ, and ψ are evaluated using the formulae in Pruppacher and Klett (1978). The rate of heat loss due to melt water evaporation is

$$F_{evap} = 2\pi D\psi\rho_a\ [q_{vs}(T_o) - q_v]\beta L_v, \tag{12}$$

where q_v and q_{vs} are the mixing ratio of the air and the saturation mixing ratio at the surface of the particle, respectively, and L_v is the latent heat of vaporization, 2.5 x 10^6 j kg^{-1}. In (12), the heat loss due to evaporation is limited by the rate of transfer of water molecules from the particle surface to the atmosphere.

$$\frac{dm_{mevap}}{dt} = \begin{cases} F_{evap}/L_v, & T > 273.16\text{K}; F_{sens} > F_{evap} \\ F_{sens}/L_v, & T > 273.16\text{K}; F_{sens} \le F_{evap} \end{cases} \tag{13}$$

In the case of rain, or if the ice particle has completely melted, evaporation of liquid is described by (Ferrier, 1994),

$$\frac{dm_{revap}}{dt} = \frac{-2\pi D(S-1)\beta}{AB}, \tag{14}$$

where the supersaturation ratio, S, is

$$S = q_v / q_{vs}, \tag{15}$$

and

$$AB = \frac{L_v^2}{K R_v T^2} + \frac{1}{\psi \rho q_{vs}}. \tag{16}$$

Also, at temperatures below freezing, sublimation/deposition of water vapor from/onto an ice particle's surface is given by (Ferrier, 1994),

$$\frac{dm_{sub}}{dt} = \frac{-2\pi D(S_i - 1)\beta}{AB_i}, \tag{17}$$

where

$$S_i = q_v / q_{vsi}, \tag{18}$$

is the supersaturation ratio with respect to ice, and

$$AB_i = \frac{L_s^2}{K R_v T^2} + \frac{1}{\psi \rho_a q_{vsi}}. \tag{19}$$

Here, q_{vsi} is the water vapor saturation mixing ratio with respect to ice, and L_s is the latent heat of sublimation, 2.83 x 10^6 j kg^{-1}.

In the processes of melting or sublimation/deposition, it is assumed that the volume proportion of air to ice in a given ice or melting particle is maintained. Therefore, at temperatures above freezing

$$\frac{dV_{am}}{dt} = -\frac{f_{ai}}{\rho_{ice}}\left[\frac{dm_{melt}}{dt}\right], \tag{20}$$

while at sub-freezing temperatures

$$\frac{dV_{asd}}{dt} = -\frac{f_{ai}}{\rho_{ice}}\left[\frac{dm_{sub}}{dt}\right], \tag{21}$$

where

$$f_{ai} = \frac{V_{air}}{m_{ice}/\rho_{ice}} \tag{22}$$

is the volume ratio of air to ice in the particle.

In addition to phase change processes, ice and melting particles can collide and combine to form aggregate particles, while pure liquid drops (rain) are immediately shed in collisions. Self-collection of raindrops is not considered here, since this process is adequately represented in the parent models, and the focus of this study is the evolution of melting precipitation particles. Which types of ice species may aggregate is determined according to microphysics of the parent model simulation (see Section 2b).

Also, in order to maintain consistency with the original definitions of the particle species, a given particle can collect another particle only if its size is greater than the collected particle. This criterion ensures that the resultant aggregate particle has material properties closer to those of the collecting particle. The rate of change in the number density, n_a , of accreted particles due to collection is given by

$$\frac{dn_a(i)}{dt} = -\sum_j \xi_{ca}(i,j)\, n_c(j) n_a(i)\, \pi \left[D_c(j) + D_a(i)\right]^2 \left|w_{Tc}(j) - w_{Ta}(i)\right| \Delta/4, \tag{23}$$

where ξ_{ca} is the collection efficiency of the particle interaction, n_c is the number density of collecting particles, D_c and D_a are the diameters of the collecting and accreted particles, respectively, w_{Tc} and w_{Ta} are the terminal velocities of the collecting and accreting particles, respectively, and Δ is the distribution diameter interval of the collecting particles. The summation is over all valid collecting particle sizes.

The total number of particles of a given size accreted by a single collecting particle per unit time is given by

$$\frac{dN_a(j)}{dt} = \xi_{ca}(i,j) n_a(j)\, \pi \left[D_c(i) + D_a(j)\right]^2 \left|w_{Tc}(i) - w_{Ta}(j)\right| \Delta/4. \tag{24}$$

It follows that the rate of change of ice and liquid water mass of a single collecting particle are

$$\frac{dm_{iacc}(i)}{dt} = \sum_j m_{a\,ice}(j)\,\frac{dN_a(j)}{dt}, \tag{25}$$

and

$$\frac{dm_{lacc}(i)}{dt} = \sum_j m_{a\,liq}(j)\,\frac{dN_a(j)}{dt}, \tag{26}$$

respectively, where $m_{a\,ice}$ and $m_{a\,liq}$ are the masses of ice and liquid water in each accreted particle, and the summations are over all accreted particles. Also, the volume of air in the collecting and accreted particles is assumed to be conserved during collection; therefore where $V_{a\,air}$ is the volume of air in the accreted particle.

$$\frac{dV_{aacc}(i)}{dt} = \sum_j V_{a\,air}(j)\,\frac{dN_a(j)}{dt}, \tag{27}$$

The combined effects of melting, sublimation/deposition, evaporation, and aggregation are now considered. For ice or melting precipitation species,

$$m_{ice}(i,z-\Delta z) = m_{ice}(i,z) + \left\{ -\delta\left[\frac{dm_{melt}}{dt}\right] - (1-\delta)\left[\frac{dm_{sub}}{dt}\right] + \frac{dm_{iacc}}{dt} \right\}\Delta t, \tag{28}$$

$$m_{liq}(i,z-\Delta z) = m_{liq}(i,z) + \delta\left\{ \frac{dm_{melt}}{dt} - \frac{dm_{evap}}{dt} + \frac{dm_{lacc}}{dt} \right\}\Delta t, \tag{29}$$

and

$$V_{air}(i,z-\Delta z) = V_{air}(i,z) + \left\{\delta\left[\frac{dV_{am}}{dt}\right] + (1-\delta)\left[\frac{dV_{asd}}{dt}\right] + \frac{dV_{aacc}}{dt}\right\}\Delta t, \tag{30}$$

where

$$\Delta t = -\Delta z/[w_T + w], \tag{31}$$

and

$$\delta = \begin{cases} 0, & T < 273.16\,\mathrm{K} \\ 1, & T \geq 273.16\,\mathrm{K}. \end{cases} \tag{32}$$

Here, Δt is the time required for the particle to fall to the next level, and w is the vertical air velocity of the particle environment. For raindrops,

$$m_{liq}(i,z-\Delta z) = m_{liq}(i,z) + \left\{-\frac{dm_{evap}}{dt}\right\}\Delta t, \tag{33}$$

which governs both completely melted ice particles and raindrops from the parent model simulation that are present at the top of the melting model domain.

The change in the number density of ice and melting precipitation particles is calculated in three steps. First, the reduction of particles due to accretion is computed;

$$n(i,z-\Delta z)' = n(i,z) + \left\{\frac{dn(i,z)}{dt}\right\}\Delta t. \tag{34}$$

Then $n(i,z\text{-}\Delta z)'$ is adjusted for the loss of particles due to evaporation or sublimation according to the governing equations (28)-(33). Since the melting model is steady-state, the number flux of particles at level z, less the flux eliminated by accretion, evaporation, or sublimation, should equal the number flux of particles at the next level. This condition is satisfied if the number flux of "surviving" particles at z, $n(i,z\text{-}\Delta z)' \bullet (w_T(i,z) + w(z))$ is set equal to the number flux at the next level, $n(i,z\text{-}\Delta z) \bullet (w_T(i,z\text{-}\Delta z) + w(z\text{-}\Delta z))$. It follows that

$$n(i,z-\Delta z) = n(i,z-\Delta z)' \frac{[w_T(i,z) + w(z)]}{[w_T(i,z-\Delta z) + w(z-\Delta z)]}, \tag{35}$$

which yields the number density of particles at the next level. Note that $w_T(i,z\text{-}\Delta z)$ is obtained from (5) using the particle composition calculated at the next level.

The foregoing equations provide a description of the melting process that is sufficient for determining the bulk electromagnetic properties of the melting layer. However, due to differences in model physics and vertical resolution, as well as the lack of horizontal advection of precipitation into or out of the one-dimensional melting model domain, the profiles of precipitation produced by the melting model may differ from those computed in the parent model. To help correct for these differences, the size distribution of each precipitation particle species in the melting model is scaled, such that the total mass flux of the resulting precipitation distributions is equal to the parent model total mass flux interpolated to the melting model grid;

$$n_{adj}(i,z) \ = \ \gamma(z)\, n(i,z), \tag{36}$$

with the scaling factor

$$\gamma(z) \ = \ \sum_{\text{species}} M_{par}(z) \Bigg/ \left\{ \sum_{\text{species}} \left[\sum_{i} n(i,z) \left(m_{ice}(i,z)+m_{liq}(i,z)\right) \left(w_T(i,z)+w(z)\right) \Delta \right] \right\}. \tag{37}$$

Here, $M_{par}(z)$ is the mass flux of a given precipitation species in the parent model interpolated to level z. From a theoretical perspective, the correction (36) may seem heavy-handed. However, the objective of the present work is to develop a description of the melting band with sufficient detail for radiative transfer calculations, and one that is compatible with the parent 3-D model simulations, as opposed to a stand-alone model. In this sense, the melting model can be viewed as a local parameterization of processes not resolved by the parent model.

Finally, from the computed ice and liquid masses and volume of air in a given particle, the volume fractions of ice, liquid, and air are calculated;

$$f_{ice}(i,z) = \frac{m_{ice}(i,z)/\rho_{ice}}{V(i,z)}, \tag{38}$$

$$f_{liq}(i,z) = \frac{m_{liq}(i,z)/\rho_{liq}}{V(i,z)}, \tag{39}$$

$$f_{air}(i,z) = \frac{V_{air}(i,z)}{V(i,z)}, \tag{40}$$

where

$$V(i,z) = \frac{m_{ice}(i,z)}{\rho_{ice}} + \frac{m_{liq}(i,z)}{\rho_{liq}} + V_{air}(i,z). \tag{41}$$

The quantities n_{adj}, f_{ice}, f_{liq}, and f_{air}, are utilized in the following sections to calculate the electromagnetic properties of melting precipitation.

b. Application to Parent 3-D Cloud-Resolving Model Simulations

In the previous section, a simplified model describing the evolution of melting precipitation was developed. Being one-dimensional, this melting model is designed to represent the melting layer at a single gridpoint in a parent, 3-D CRM simulation and is driven by the distributions of ice precipitation just above the freezing level in the parent simulation. In this section the parent model simulations are briefly described, and applications of the melting model to a single parent model profile are presented. The 3-D CRM model runs serve as the basis of the melting simulations described in the following section as well as the simulated radiance and radar reflectivity fields in Part II.

The parent model simulations of this study are derived from the Goddard Cumulus Ensemble (GCE) model and the University of Wisconsin Non-hydrostatic Modeling System (UW-NMS); see Table 1. A detailed description of the GCE model may be found in Tao and Simpson (1993). The GCE model is non-hydrostatic, with cloud microphysics described by an adaptation of the Lin et al. (1983) scheme. In this scheme, precipitating particle distributions are represented by inverse exponential distributions with fixed intercepts; the slopes of the distributions are adjusted to account for changes in water content, which are computed prognostically. The particle material densities in this scheme are also fixed: rain has a density of 1.0 g cm^{-3}, while snow and graupel have densities of 0.1 and 0.4 g cm^{-3}, respectively. Three GCE model simulations are utilized in the present work. Two of these simulations are initialized using temperature, humidity, and wind conditions observed 22 February 1993, during the Tropical Ocean-Global Atmosphere Coupled Ocean Atmosphere Response Experiment (TOGA COARE). A tropical squall line observed to the southwest of the TOGA COARE

Intensive Flux Array (IFA) was simulated on a 1 km, 128 x 128 grid (TOGA1) and a 3 km, 128 x 128 grid (TOGA3). Both squall lines were initiated with a spreading cool pool centered in the model domain that generated a gust front-like forcing. A third simulation is derived from a long-term, forced simulation of convection in the TOGA COARE IFA during the period 19-26 December, 1992. The extensive mesoscale convective system that occurred on 24 December is represented in the simulated 12 UTC precipitation field on a 2 km, 256 x 256 grid (TOGA2).

The UW-NMS is described in Tripoli (1992a). The microphysical scheme employed is from Flatau et al. (1989), with specified parameters tabulated by Panegrossi et al. (1998). In the simulations utilized in the present study, the precipitating hydrometeor species have inverse exponential size distributions, but unlike the GCE model, the slopes of these distributions are fixed, while the intercepts are allowed to vary with water content. Rain and graupel have fixed material densities of 1.0 and 0.6 g cm^{-3} respectively, while snow has a size-dependent density given by

$$\rho_{m-snow} = 0.0597\, D^{-0.6}, \qquad (42)$$

where the particle diameter D is in mm, and the resulting density is in g cm^{-3}. Two UW-NMS simulations are used in the current study. The first is a simulation of a thunderstorm complex observed during the Cooperative Huntsville Meteorological

Experiment. Identified here as COHMEX, this simulation was performed on a 1 km, 51 x 51 grid domain. A description of COHMEX can be found in Mugnai et al. (1990). A second simulation was initialized with a balanced vortex and sounding data from the environment preceding the passage of Hurricane Gilbert (1988) at Kingston, Jamaica. The resulting hurricane simulation (hereafter, HURRICANE) was performed on a two-way, quadruply-nested grid, which included a 3.3 km resolution, 62 x 62 inner nest during the last 6 hours of simulation time to resolve the inner core region of the storm. Details of HURRICANE may be found in Tripoli (1992b).

Depicted in Fig. 2 is a plan view of the surface rainfall rate field in the TOGA1 tropical squall line simulation at 180 min into the simulation. On the right side of the figure is the bowed convective leading edge of the squall line with rain rates exceeding 16 mm h^{-1}. The leading-edge convection extends to the south and west (north is up in the Figure). Less intense and more horizontally uniform stratiform precipitation trails the convection to the north and west.

The crossing of the dotted lines at $x = 42$ km and $y = 75$ km in Fig. 2 indicates the position of the test profile examined in this section. This gridpoint is located near the center of an area of stratiform rain, with a surface rainfall rate of 0.6 mm h^{-1}. The melting layer model is applied to the TOGA1 simulation at the gridpoint. The top of the melting layer model coincides with the 6 km level in the parent model simulation, where the temperature is just below freezing (271.4 K), and the snow and graupel water contents are

0.17 g m^{-3} and 0.25 g m^{-3}, respectively. The freezing level occurs 0.37 km below the melting model top.

Presented in Fig. 3a and b are the liquid water content and mass flux profiles, respectively, of snow, graupel, rain, and total precipitation calculated using the melting model. Note that in order to emphasize the melting model physics, subsequent scaling of the precipitation mass flux using (36) is omitted in this example. From the top of the model domain to the freezing level, sublimation of ice reduces the mass and mass flux of both snow and graupel, while aggregation processes are weak (collection efficiency is less than 0.1). The melting of ice-phase particles falling below the freezing level is initially inhibited by the evaporation of meltwater [see (12)], a process that consumes most of the sensible heat flux to each particle while removing little mass. More effective aggregation at these temperatures (collection efficiency of 1.0) causes a slight increase in the water content of snow while the water content of graupel decreases; however, the total mass flux of snow and graupel together is nearly constant from the freezing level to a depth of 0.75 km (about 0.4 km below the freezing level).

Below a depth of 0.75 km, the increasing humidity of the air effectively shuts off meltwater evaporation, and the increasing sensible heat flux from the air causes rapid melting of snow and graupel. The denser graupel particles do not melt as quickly as snow of the same size, and the graupel completely melt at a depth 0.25 km lower than snow. The melted and partially–melted snow and graupel attain higher terminal velocities, and therefore the total water content of precipitation decreases rapidly with melting, despite the fact that the total mass flux of precipitation is nearly constant. . At 1.8 km depth the snow and graupel are completely melted, and the gradual decrease of precipitation water content and mass flux below this level is caused by the evaporation of rain.

One of the limiting assumptions in the GCE model microphysics is that both snow and graupel particles have material densities independent of particle size. Studies by Locatelli and Hobbs (1974), Mitchell et al. (1990), and others suggest that the density of snow particles decreases markedly with size, while graupel particles show only a slight decrease in density with size. The snow density relationship of Mitchell et al. (1990), and a curve fit to the graupel observations of Locatelli and Hobbs (1974) yield

$$\rho_{m-snow} = 0.149\, D^{-1.0}, \tag{43}$$

and

$$\rho_{m-graupel} = 0.144\, D^{-0.341}, \tag{44}$$

where D is in mm and $\rho_{m\text{-}snow}$ and $\rho_{m\text{-}graupel}$ are in g cm^{-3}. Snow and graupel with these density distributions are substituted for the snow and graupel distributions at 6 km at the same gridpoint of the TOGA1 simulation, and the number densities of both types of particles are scaled to yield the same water contents as those in the original simulation.

The modified snow and graupel distributions are then used to initialize the melting model, with the resulting profiles of precipitation water contents and mass fluxes shown in Figs. 3c and 3d, respectively.

Comparing the model profiles to the profiles based upon the fixed-density model in Figs. 3a and 3b, it may be noted that the primary difference is the more rapid melting of the variable density particles. The depth of the melting layer contracts from about 1.0 km to 0.5 km. This result is due to the more rapid melting of the larger snow and graupel particles, which are less dense than their constant-density counterparts. These larger particles require the most time to completely melt and therefore limit the melting time of the distribution. The differences in melting rate will have an impact on the radiometric properties of the melting band, to be discussed in Section 2c.

c. Dielectric Properties of Melting Hydrometeors

i. Maxwell-Garnett Model

Generally, the effective dielectric constant of an inhomogeneous particle is calculated as a function of the individual contributions by ice, water, and air. The most widely used formulation follows the Maxwell-Garnett approach (Maxwell-Garnett 1904) which was generalized by Bohren and Battan (1982). An inhomogeneous particle is described as a matrix material with randomly distributed and oriented elliptical inclusions which contribute to the effective dielectric constant of particle in proportion to their volume fraction, f_{inc}.

$$\varepsilon_{mix} = \frac{[1-f_{inc}]\varepsilon_{mat} + f_{inc}\zeta\varepsilon_{inc}}{1-f_{inc}+f_{inc}\zeta}, \tag{45}$$

where

$$\zeta = \left[\frac{2\varepsilon_{mat}}{\varepsilon_{inc}-\varepsilon_{mat}}\right]\left\{\left[\frac{\varepsilon_{inc}}{\varepsilon_{inc}-\varepsilon_{mat}}\right]\ln\left(\frac{\varepsilon_{inc}}{\varepsilon_{mat}}\right) - 1\right\}. \tag{46}$$

Here, ε_{mat}, ε_{inc}, and ε_{mix}, denote the complex dielectric constant of the matrix, the inclusions, and the mixture, respectively, and $\ln(\varepsilon_{inc}/\varepsilon_{mat})$ is the principal value of the complex number $\varepsilon_{inc}/\varepsilon_{mat}$. For three component mixtures, (45) must be applied twice, and the resulting dielectric constant of the mixture depends upon the order of application as well as the choice of matrix and inclusion materials in each application.

ii. Meneghini and Liou Models

Several intercomparisons of available dielectric model formulations have been carried out, including (45) and others that treat the mixture as a homogeneous composite. Klaassen (1988) demonstrated that even homogeneous formulations such as Debye (1929), Bruggeman (1935), and Maxwell-Garnett (1904) deviate strongly from one another. To test these formulations, Meneghini and Liao (1996) solved the electromagnetic field equations numerically for particles subdivided into a grid of cells containing ice, air, or water. The effective dielectric constants of the particles were then determined as those which, when input to Mie theory, produced the same extinction and backscattering coefficients as the numerical technique.

For particles containing homogeneous distributions of ice, air, and water, the effective dielectric constants were well-approximated by the Maxwell-Garnett formula for water inclusions in an ice matrix, ε_{MGiw} (hereafter referenced as MGiw), for ice volume fractions greater than 0.2. The Maxwell-Garnett formula for ice inclusions in a water matrix, ε_{MGwi} (hereafter referenced as MGwi) compared best to their numerical method when the ice volume fraction was less than 0.2. On the other hand, if meltwater accumulated at the particle surface, the effective dielecric constant was again well represented by ε_{MGwi}. The distribution of meltwater within the particle, however, depends upon the initial particle density and melting stage; therefore, different dielectric models may be optimal for a given particle density and melting stage.

For a spatially homogeneous ice-water mixture, i.e., meltwater pockets randomly distributed throughout the particle volume, Meneghini and Liou (1996) developed an analytical function to better represent the particle dielectric constant, e_{ML96} (hereafter referenced as ML96), at a frequency of 7.7 GHz. At intermediate melting stages they utilized an error function to interpolate between the dielectric constant of an ice-air matrix with water inclusions, ε_{MGiw} (initial melting stage), and that of a water matrix with ice-air inclusions, ε_{MGwi} (later melting stage), as a function of the fractional volume of ice, f_{ice}.

$$\varepsilon_{ML96} = 0.5\left\{\left[1-\operatorname{erf}(\xi)\right]\varepsilon_{MGwi} + \left[1+\operatorname{erf}(\xi)\right]\varepsilon_{MGiw}\right\}, \qquad (47)$$

where the error function is defined as

$$\operatorname{erf}(\xi) = \frac{2}{\sqrt{\pi}}\int_0^{\xi}\exp\left(-\psi^2\right)d\psi, \qquad (48)$$

and

$$\xi = \frac{\left[f_{ice}/\left(1-f_{ice}\right) - \vartheta_1\right]}{2\vartheta_2}. \tag{49}$$

The parameters $\vartheta_1 = 0.2$ and $\vartheta_2 = 0.1$ yield a good approximation to the effective dielectric constants determined from their numerical technique.

The application of the ML96 formula to frequencies other than 7.7 GHz may not seem justified, but the effective dielectric constant calculation is driven by the weights obtained from the error function which are closely tied to ε_{MGiw} at early melting stages and thus represent a rather conservative estimate of the dielectric constant. Also, the ML96 formula was applied only to mixtures of pure ice and liquid water. In the present study $f_{ice} + f_{air}$ is substituted into (49) for f_{ice}, where the Maxwell-Garnett formula for air inclusions in an ice matrix is used to compute the dielectric constant of the ice-air mixture.

More recently, Meneghini and Liao (1997; hereafter referenced as ML97), improved the numerical accuracy of their dielectric constant calculations, employing a continuous, multiple-component particle approach with parameterizations which allow for applications to frequencies between 10 and 95 GHz. Their model was based upon the assumption that the properties of the particle constituents are homogeneous, isotropic, and linearly superimposed. Therefore,

$$\varepsilon_{ML97} = \frac{\varepsilon_{liq} f_{liq} \frac{\langle E_{liq} \rangle}{\langle E_{ice} \rangle} + \varepsilon_{air} f_{air} \frac{\langle E_{air} \rangle}{\langle E_{ice} \rangle} + \varepsilon_{ice} f_{ice}}{f_{liq} \frac{\langle E_{liq} \rangle}{\langle E_{ice} \rangle} + f_{air} \frac{\langle E_{air} \rangle}{\langle E_{ice} \rangle} + f_{ice}}, \qquad (50)$$

where ε_{ice}, ε_{air}, and ε_{liq} represent the permittivities of pure ice, air and water with volume fractions f_{ice}, f_{air}, and f_{liq}, respectively. The terms in brackets denote the average electric fields, assuming that the particle can be decomposed into individual cells over which the fields are homogeneous. Therefore, the summation of all cell contributions to the total field is equivalent to the average field multiplied by the number of cells. The ratio of the average electric fields in (50) is computed from the Debye formula assuming a dry "snow" particle with $f'_{ice} + f'_{air} = 1$,

$$\frac{\langle E_{air} \rangle}{\langle E_{ice} \rangle} = \frac{f'_{ice} \left[\varepsilon_{dry} - \varepsilon_{ice} \right]}{f'_{air} \left[\varepsilon_{air} - \varepsilon_{dry} \right]}, \qquad (51)$$

where

$$\varepsilon_{dry} = \frac{\rho_{ice} + 2 \kappa_{ice} \rho_{dry}}{\rho_{ice} - \kappa_{ice} \rho_{dry}}, \qquad (52)$$

$$\kappa_{ice} = \frac{\varepsilon_{dry} - 1}{\varepsilon_{dry} + 2}, \qquad (53)$$

and

$$\rho_{dry} = \frac{m_{ice}}{\frac{m_{ice}}{\rho_{ice}} + V_{air}} \qquad (54)$$

is the density of the dry "snow" particle. Finally, both the real and imaginary parts of $\langle E_{liq}\rangle/\langle E_{ice}\rangle$ were computed by ML97 using a conjugate gradient numerical method and parameterized as functions of frequency and fractional meltwater.

iii. Concentric Shell Models

Another approach to the problem of approximating the dielectric properties of a melting ice particle is to construct it from concentric shells of material with different dielectric properties. The most common example is a water-coated sphere, which may be a sufficient approximation for melting hailstones or graupel with high material densities. Regarding snow particles, a more detailed description of each layer is required, and this may be obtained through the application of (45) to each shell.

Shivola and Lindell (1989) developed the theoretical background for various dielectric constant profiles through inhomogeneous particles. Their work allowed a more sophisticated treatment of continuous dielectric constant variations as a function of radius within the particle. The assumed density and dielectric discontinuities in a shell model represent a simplification of their approach which seems justified in view of the lack of knowledge regarding the spatial variations of density and composition as a function of radius in melting particles.

For the purpose of modeling radar reflectivities in the melting layer, Fabry and Szyrmer (1999; hereafter FS) implemented a core-shell model which was then incorporated into the framework of a microphysical melting model by Szyrmer and Zawadski (1999). In their model, the particle core consists of ice inclusions in a water matrix, which together serve as a matrix for air inclusions. The latter are treated as bubbles in a comparatively solid environment. The outer shell is modeled as ice inclusions in a water matrix, which together form inclusions in a matrix of air. Thus the outer shell represents a rather tenuous collection of melting ice crystals. The dielectric constants of the core and shell are calculated using (45).

FS compared modeled and observed radar reflectivities at 0.9 and 9.4 GHz and obtained better agreement using this approach in relation to alternative models based upon (45) for different choices of matrix and inclusion materials. FS confirm that the use of (45) with a water matrix showed an exaggeration of the melting layer reflectivity, a result in concert with studies by Bauer et al. (1999a,b), who noted excessive microwave emission from the modeled melting layer when (45) with the water matrix assumption was applied. Moreover, these authors concluded that the choice of a particle dielectric constant model outweighs other sources of uncertainty such as the assumption of particle density.

Crucial to the FS model is the calculation of particle density change with melting stage and the position of the boundary between the particle core and outer shell. Prior to melting, the core and outer shell densities of the dry snow particle are

$$\rho_{dry,core} = \rho_{dry}\,\alpha_{dry}^{-1}, \tag{55}$$

and

$$\rho_{dry,shell} = \rho_{dry}\frac{\left(1-\alpha_{dry}^{2}\right)}{\left(1-\alpha_{dry}^{3}\right)}, \tag{56}$$

where α_{dry} is the radius of the core region expressed as a fraction of the total radius of the particle. Note that (55) and (56) may be derived assuming that density is a continuous function of 1/radius within the particle; then $\rho_{dry,\,core}$ and $\rho_{dry,\,shell}$ are the average densities within the particle core and shell, respectively. The bulk material density of a particle with these core and shell densities is equal to ρ_{dry}, regardless of the α_{dry} chosen. In FS, $\alpha_{dry} = 0.5$ in (55) and (56). During melting, the densities of the core and shell regions change according to

$$\rho_{m,core} = \frac{\rho_{dry,core}\,\rho_{liq}}{f_{mliq}\,\rho_{dry,core} + \left(1 - f_{mliq}\right)\rho_{liq}}, \tag{57}$$

and

$$\rho_{m,\ shell} = \frac{\rho_{dry,shell}\,\rho_{liq}}{f_{mliq}\,\rho_{dry,shell} + \left(1 - f_{mliq}\right)\rho_{liq}}, \tag{58}$$

respectively, where

$$f_{mliq} = \frac{m_{liq}}{m_{ice} + m_{liq}}, \tag{59}$$

the mass fraction of melt water, is assumed to be the same in both the core and shell regions. Under these conditions, the core radius fraction of the particle is

$$\alpha = \left[\frac{\rho_m - \rho_{m,shell}}{\rho_{m,core} - \rho_{m,shell}}\right]^{1/3}, \tag{60}$$

where ρ_m is the average density of the particle, given by (6). As the particle melts, the core and shell densities approach 1 (completely melted), and the core radius fraction also approaches 1 (the melted particle radius).

If the core region of the particle is treated as a spherical inclusion within a matrix of shell material, the effective dielectric constant of the complete particle can be approximated by the original Maxwell-Garnett theory. Under this assumption the effective dielectric constant is

$$\varepsilon_{FS} = \varepsilon_{shell} + \frac{3\varepsilon_{shell}\alpha^3\left[\varepsilon_{core}-\varepsilon_{shell}\right]}{\varepsilon_{core}+2\varepsilon_{shell}-\alpha^3\left[\varepsilon_{core}-\varepsilon_{shell}\right]}, \tag{61}$$

where ε_{core} and ε_{shell} are the permittivities of the core and shell regions, respectively. However, (61) is only appropriate if the particle dimensions are small compared to the wavelength of radiation, a condition that is not always satisfied in the present application. The rigorous alternative is to calculate the particle radiative properties by solving the electromagnetic field equations for a two-shell system, as in Bohren and Huffman (1983). This alternative will be explored in Section 2d.

iv. Intercomparison of Dielectric Constant Models

Particle dielectric constants at 10.65, 19.35, 37.0, and 85.5 GHz are calculated for melting snow (initial $\rho_m = 0.1$ g cm^{-3}) and graupel (intial $\rho_m = 0.4$ g cm^{-3}) and converted to refractive indices using

$$n = \sqrt{\varepsilon}. \tag{62}$$

Melting snow and graupel refractive indices are presented in Figs. 4 and 5, respectively. The five curves in each panel correspond to calculations using the different dielectric models described in the previous subsection. The curves converge to points near the lower left (no meltwater) and upper right (completely melted) corners of each panel, with a "+" indicating a meltwater volume fraction of 0.5.

It may be noted from the figures that the refractive index curves are generally bounded by the MGwi and MGiw model curves. The quasi-linear MGwi curve yields the maximum rate of increase of the imaginary component of refractive index with melting. Conversely, the MGiw model typically yields the smallest rate of increase of the imaginary component. The other three models tend to follow the behavior of MGiw but with noted differences. ML96 closely follows MGiw up to a volume meltwater fraction of 0.5, but then it makes a transition to MGwi for higher meltwater fractions. The ML97 model yields imaginary refractive indices sometimes even lower than those produced by MGiw for very low meltwater fractions, but then gradually diverges from the MGiw curve for higher meltwater fractions. In contrast, the FS model yields a higher imaginary refractive index component than either ML96 or ML97 for meltwater fractions less than

0.5, but then approaches the MGiw model refractive index as the meltwater fraction increases from 0.5 to 1.0.

The refractive indices of snow and graupel are subtley different. A close inspection of Figs. 4 and 5 reveals greater real and imaginary refractive index components for graupel with a given meltwater fraction for all but the MGwi model. The MGwi model yields slightly smaller refractive indices for graupel relative to snow. Overall, the refractive index differences between snow and graupel decrease as the meltwater fraction increases.

Since the radiative absorptivity of a material increases with the imaginary component of the refractive index, pure snow or graupel are expected to be poor absorbers. Once snow or graupel begin melting, the MGwi model would produce the greatest increase in absorptivity with meltwater fraction. As mentioned earlier, the MGwi model may exaggerate the radiative effect of melting except for relatively dense particles (graupel or hail) for which meltwater may initially accumulate near the surface of the particle. The more rigorous ML97, which describes the dielectric properties of particles with homogeneously-distributed meltwater, may also be applicable to denser ice particles, but the absorptivity of the particles would generally be less. Snow, having an ice-air density which decreases with radius within the particle, is more appropriately described by the FS, core-shell model. The bulk refractive index of snow based upon FS indicates significantly greater absorptivity for low meltwater fractions in comparison to ML97 or

MGiw, but less absorptivity for higher meltwater fractions. The impact of dielectric constant models on the radiative properties of melting ice particles is next examined.

d. Radiative Properties

Plotted in Fig. 6 are the absorption and scattering efficiencies of the FS melting particles at 10.65, 19.35, 37.0, and 85.5 GHz. The efficiencies are calculated based upon the analytical solution for electromagnetic waves interacting with a dielectric sphere having a core and outer shell (ref. Bohren and Huffman, 1983). The absorption and scattering efficiencies, multiplied by a particle's geometric cross section, are proportional to the radiative power absorbed and scattered by the particle at these TMI channel frequencies. Presented in each plot are efficiency curves for five different meltwater water volume fractions spanning the range from "dry" snow ($\rho_{ice\text{-}air} = 0.10$ g cm^{-3}) to pure liquid composition. At all frequencies, and for all particle compositions, the efficiencies increase with increasing particle size until the particle radius is approximately equal to the wavelength of radiation. At larger particle radii, maximum efficiencies are first attained by the pure liquid particles, and then by particles with decreasing meltwater fractions. Dry snow particles have very low absorption and scattering efficiencies, with the exception of relatively large particles at 37.0 and 85.5 GHz.

For relatively small volume fractions of meltwater (less than ~0.10), absorption and scattering efficiencies of the particles generally increase with meltwater fraction. The increase of efficiency with meltwater fraction is greatest for the smallest meltwater fractions, a nonlinear sensitivity that has been noted by other investigators; e. g. Meneghini and Liao (1996). Note that the absorption efficiencies of particles that are relatively large with respect to wavelength attain maximum values for intermediate meltwater fractions (~0.4), while the efficiencies of pure liquid drops of the same size are less. The same trend is not seen in particle scattering efficiencies, which nearly always increase with increasing meltwater fraction. The implication of these trends is that the radiometric absorption/emission and scattering of only slightly melted particles can be significant compared to pure liquid drops of the same size, and that the absorption/emission of particles with significant melted fractions can actually exceed that of pure liquid drops.

The individual particle properties are integrated over the size distribution of each particle species in the test profiles depicted in Fig. 3a to produce the profiles of bulk absorption and scattering coefficients in Figs. 7a and 7b, respectively. These bulk absorption and scattering coefficients are based upon application of the FS, core-shell dielectric model to both snow and graupel. For comparison, absorption and scattering coefficients based upon the MGwi model are plotted in Figs. 7c and 7d, respectively.

It may be inferred from Fig. 7a that the bulk absorption by melting snow and graupel is greater than the absorption by rain alone at the base of the melting layer. The higher water contents of precipitation (Fig. 3a) as well as the elevated absorption efficiencies of partially melted precipitation (Figs. 6a, c, e, and g) contribute to greater absorption in the melting layer. Maximum absorption occurs just below the freezing level based upon the FS, core-shell model, and it is about an order of magnitude greater than the absorption by rain below the melting layer at 10.65 GHz. Maximum absorption is about 5, 3 and 2 times the absorption by rain at 19.35, 37.0 and 85.5 GHz, respectively. Microwave scattering is also maximized in the melting layer. However, at frequencies less than 85.5 GHz scattering is generally much less than absorption, and the scattering peaks are broader, extending through the depth of the melting layer (Fig. 7b). The broader scattering peaks result from the less rapid, monotonic increase of scattering efficiency with melted particle fraction, as seen in Figs. 6b, d, f, and h, whereas the absorption efficiency increases more rapidly with melted fraction for a wide range of particle sizes (Figs. 6a, c, e, and g). At 85.5 GHz, absorption and scattering in the melting layer are comparable. The absorption and scattering coefficients based upon the MGwi model exhibit similar trends, with a slightly higher and narrower peaks of absorption given by MGwi. The scattering profiles produced by the two models are nearly identical.

In Fig. 8, the extinction efficiency and normalized backscatter cross-section based upon the FS, core-shell model are plotted for particles with various volume fractions of meltwater at 13.8 GHz, the operating frequency of the PR. The extinction efficiency, multiplied by the particle's geometric cross-section, is proportional to the radar attenuation by the particle. Similarly, the normalized backscatter cross-section multiplied by the particle geometric cross-section is proportional to the radar power reflected by the particle. The extinction efficiencies at 13.8 GHz (Fig. 8a) follow the same trends as the absorption efficiencies at 10.65 GHz (Fig. 6a). It may be inferred that radar attenuation becomes significant with the onset of particle melting. On the other hand, particle backscatter cross-sections increase almost in proportion to the particle melted fraction.

The individual particle extinction efficiencies and backscatter cross-sections are integrated over the size distribution of each particle species in the test profiles depicted in Fig. 3a to produce the profiles of bulk extinction coefficient and radar reflectivity in Fig. 9a and 9b, respectively. These profiles are based upon the FS, core-shell dielectric model, and the contributions from snow, graupel, and rain are indicated. For comparison, extinction coefficients and radar reflectivities based upon the MGwi model are plotted in Figs. 9c and 9d, respectively.

Since microwave scattering is almost negligible in comparison to absorption at 13.8 GHz, the profiles of total extinction have almost the same form as the profiles of absorption shown in Fig. 7a. Note that the peak extinction by snow is almost the same as that of graupel, even though the water content of graupel is always greater than that of snow (Fig. 3a). This result is explained by the greater proportion of large particles, which have greater extinction efficiencies, in the snow distribution according to the GCE model microphysics. The greater proportion of large snow particles offsets the slightly greater extinction efficiency of graupel. On the other hand, due to their lower density, snow particles melt more rapidly than graupel particles of the same size, leading to a relatively narrow peak of snow extinction. The peak reflectivity of the melting band reaches nearly 37 dBZ about 0.6 km below the freezing level, where the slower-melting graupel makes a greater contribution to the reflectivity. The peak reflectivity of the melting layer greatly exceeds the reflectivity of rain below the melting layer (~27 dBZ). Note also that the peak of reflectivity is at a slightly lower altitude than the peak of extinction. This effect is explained by the more gradual increase of backscatter efficiency (relative to extinction efficiency) with meltwater fraction; see Fig. 8. The greater refractive indices produced by the MGwi model for melting particles leads to generally greater extinction and reflectivity of the melting layer (Figs. 9c and 9d). Ice species with initial densities which decrease with size (Fig. 3c, d) melt more rapidly, resulting in narrower peaks of extinction and reflectivity (Fig. 10a, b).

3. Comparison of Melting Band Simulated Attenuation to Radar Observations

The aspect of the melting band model which is perhaps most relevant to radiometer and radar remote sensing of precipitation is whether or not the model can simulate the extinction of microwave radiances. In the previous section it was demonstrated that radiative absorption and scattering per kilometer within the melting layer could be several times the absorption and scattering of the fully melted precipitation below. This absorption and scattering could have an impact on the upwelling radiances measured by passive microwave radiometers. Similarly, the additional extinction in the melting layer could lead to greater attenuation of reflectivities below the layer, as observed by spaceborne radar.

Here, the radar "mirror-image" technique (ref. Liao et al., 1999) is applied to observations of the Precipitation Radar (PR) in stratiform rain areas to estimate the radiative extinction associated with melting precipitation. A schematic of a PR reflectivity profile is provided in Fig. 11 for the identification of specific reflectivity measurements described in the analysis. Mirror-image reflectivities refer to reflectivities measured at ranges beyond the range of the surface reflection. These reflectivities are produced by radar pulses that have reflected off the earth's surface, are then backscattered by a precipitation target, and are finally reflected off the earth's surface a second time toward the radar receiver. The present application of the technique to PR observations follows.

First, nadir-view reflectivity profiles and derived products from the PR are collected from the period August 4 – 22, 1998, over the region bounded by 20 °S and 20 °N latitude, 180 °W and 120 °W longitude. The data are filtered using the qualitative flags in the derived TRMM product 2A-23 (Awaka et al. 1998) to select only profiles where stratiform rain was present and a radar bright band was detectable. The reflectivities of each three consecutive nadir profiles are averaged to reduce noise for subsequent processing. The averaged profiles are next analyzed to identify the bright band reflectivity bin (maximum reflectivity bin within 1.5 km of the maximum reflectivity gradient above the rain layer). The range difference between the radar surface return and the bright band is calculated, and then the bright band "mirror image" bin is identified as the maximum reflectivity bin within 0.75 km of an equal range displacement beyond the surface return. If either the bright band reflectivity (Z_{bb})or its mirror image reflectivity ($Z_{bb\text{-}m}$) are below 25 dBZ, the profile is rejected. An alternate surface range is defined as the average of the range of the bright band range and the bright band mirror image range. If this surface range deviates by more than 0.125 (half a range bin) from the range of the maximum surface return, then the profile is rejected. A "basal" reflectivity (Z_{ba}) and a "basal-mirror" reflectivity ($Z_{ba\text{-}m}$) are then identified as those corresponding to bins 1.5 km below the bright band and its mirror image, respectively. Also, a "reference" reflectivity (Z_{rf}) and a "reference-mirror" reflectivity ($Z_{rf\text{-}m}$) are identified as those of bins 0.75 km before and 0.75 km beyond the alternate surface range. If any of the reflectivities of the basal, basal-mirror, reference, or reference-mirror are less than 20 dBZ, the profile is rejected. The purpose of the filtering process is to remove profiles which (a) do not have an easily identifiable bright band or bright band mirror image, (b) have uncertain bright band or mirror image bright band ranges relative to the surface range, and (c) do not have basal, basal-mirror, reference, and reference-mirror reflectivities which are significantly greater than minimum-detectable (~17 dBZ).

Profiles that survive the filtering process are analyzed to estimate the optical depth between the bright band height and the level 1.5 below the bright band. Although it may be argued that the bulk of the extinction due to melting, based upon Figs. 9 and 10, lies between the top of the bright band and a kilometer below the top, application of the mirror-image technique requires well-defined reference levels, and reflectivity measurements that are relatively noise-insensitive. Radar reflectivities above the bright band maximum are often close to minimum-detectable, and the bright band maximum and its mirror-image supply well-defined height references. A 1.5 km layer depth ensures that the melting process is entirely contained within the layer, and puts the base reflectivity and its mirror image below the gradient region associated with melting, establishing a more certain reflectivity reference.

Following Liao et al. (1999), the reflectivity double-differences are defined

$$\Omega_{bb} = \left(Z_{bb} - Z_{bb-m}\right) - \left(Z_{rf} - Z_{rf-m}\right), \tag{63}$$

and

$$\Omega_{ba} = \left(Z_{ba} - Z_{ba-m}\right) - \left(Z_{rf} - Z_{rf-m}\right), \tag{64}$$

where all reflectivities are in dBZ. For ideal, beam-filling radar targets and specular reflection of the nadir-view radar beam off a flat ocean surface, the measured difference

Ω_{bb} would be four times the radar path attenuation (4-way attenuation) between the bright band and the 0.75 km altitude reference level. Similarly, Ω_{ba} would be the 4-way attenuation between the base level and the reference level. For wind-roughened ocean surfaces, Liao et al. (1999) *modeled* the 4-way attenuation between any altitude h and a reference level of 0.75 km, corresponding to a PR-measured double-difference Ω and surface radar backscatter cross-section, σ^o. These 4-way attenuation simulations were fit to an empirical function, $\Gamma[\Omega, h, \sigma^o]$. Using this function, measurements Ω_{bb} and Ω_{ba}, and an estimate of the surface backscatter cross-section σ^o from nadir-view PR measurements in rain-free regions (TRMM 1C21 product; Meneghini et al. 1999), the optical depth, τ, between the bright band and base level can be estimated from

$$\tau = \frac{\ln(10)}{40}\left\{\Gamma\left[\Omega_{bb}, h_{bb}, \sigma^o\right] - \Gamma\left[\Omega_{ba}, h_{bb} - 1.5\ \mathrm{km}, \sigma^o\right]\right\}, \qquad (65)$$

where h_{bb} is the altitude of the bright band.

Equation (65) is applied to the filtered PR reflectivity profile data from August, 1998, and the resulting estimates of τ are plotted versus corrected basal reflectivity measurements, Z^*_{ba}, in Fig. 12. The basal reflectivities are corrected using

$$Z^*_{ba} = Z_{ba} + \frac{20}{\ln(10)}\tau, \qquad (66)$$

where the reflectivities are evaluated in dBZ. The correction, (66), compensates for the attenuation of the basal reflectivity due to overlying precipitation between the basal level and the bright band. This correction makes Z^*_{ba} a parameter representative of the "output" precipitation below the melting layer which is more or less independent of optical depth variations in the precipitation above. In this way, the impact of optical depth variations in the melting layer are seen primarily along the optical depth axis of the plots in Fig. 12. Error bars are calculated based upon the estimated uncertainties in the PR reflectivity data, the altitudes of the bright band and basal reflectivity bins, and the surface backscatter cross-section. Since the error bars do not vary greatly over the distribution of plotted values, they are plotted for only one representative point in each panel.

Also plotted in the different panels of Fig. 12 are the optical depths corresponding to corrected basal reflectivities calculated using the melting layer model developed in the present study. The melting model profiles are initialized using the snow and graupel water contents just above the freezing level in stratiform areas of the TOGA1 and TOGA3 model simulations. Four variations of the melting layer simulations are represented in the figure. First, a melting simulation in which partially melted ice hydrometeors are "refrozen", such that the meltwater is converted to an ice-air mixture with the same material density as the remainder of the frozen particle. Only when a snow or graupel particle is completely melted is it converted to pure liquid (raindrop). This first simulation therefore represents a control in which the dielectric properties of mixed-phase, partially-melted ice particles are not considered. In a second melting simulation the dielectric properties of snow are described by the FS core-shell model, and graupel dielectric properties are described by the MGwi model. A third melting simulation again incorporates the FS core-shell model for snow, but substitutes the ML97 model for graupel. A fourth simulation incorporates the FS core-shell and MGwi models for snow and graupel, respectively, but alters the density distributions of snow and graupel according to (43) and (44).

Even considering the uncertainties in the PR-observed optical depths, Fig. 12 indicates a significant range of melting layer optical depths corresponding to corrected basal reflectivities between 25 and 40 dBZ. Optical depths between 0.025 and 0.35 are derived from the mirror-image technique, and there is a trend of higher optical depths with higher basal reflectivities. In contrast, the melting model containing no mixed-phase particles (Fig. 12a) produces systematically lower optical depths for a given basal reflectivity. This systematic difference can be partly explained by the uncertainty in the observed optical depths and natural variations in precipitation particle size distributions that are not represented in the melting model. Since the current melting model does not include a description of the evolution of the rain drop-size spectrum, the issue of varying particle distributions cannot be fully addressed here.

However, the presence of mixed-phase, melting ice hydrometeors can at least partly explain the observed optical depth distribution. Plotted in Fig. 12b are the optical depth - corrected basal reflectivity pairs from the melting model simulation based upon the FS core-shell model for snow and the MGwi model for graupel. Note that there is a much greater breadth of optical depths produced by this simulation and much greater overlap with the observed distribution of optical depths, in comparison to the simulation without mixed-phase particles. The greater overlap of the distributions is the result of two effects: first, there is a general increase in the optical depths of the simulated melting layers due to absorption by mixed-phase particles; second, the corrected basal reflectivities are slightly lower due to greater attenuation by precipitation above the bright band. Still, in the observed distribution at lower basal reflectivities there are a few relatively high melting layer optical depths that are not explained by the FS/MGwi simulation.

If the ML97 model is substituted for MGwi to describe the dielectric properties of graupel (Fig. 12c), somewhat lower optical depths result, but these are still generally higher than those produced by the model with no mixed-phase particles. Even though ML97 provides a fairly rigorous description of homogeneous melting particles, the radiative extinction produced by these particles appears to be insufficient to explain the observed optical depths. Snow and graupel particles with empirical size-dependent densities are substituted for the constant-density particles from the GCE parent simulations to obtain the modeled optical depths and basal reflectivities of Fig. 12d. Note that the modeled optical depths have a greater spread than those produced by the constant-density particles at basal reflectivities less than about 33 dBZ, and they are generally lower than those produced by the constant-density particles at higher basal reflectivities. A simple explanation of these distributions is difficult, since the variable-density particles generally produce shallower melting layers with smaller optical depths, but at the same time, corrected basal reflectivities are also reduced (Fig. 9a, b vs. Fig. 10a, b). Overall, the optical depth distributions from the constant- and variable-density particles are quite similar.

Although the foregoing analysis does not confirm the validity of any particular melting model simulation, it does suggest that greater consistency between observed and simulated radiative properties of the melting layer can be achieved when the dielectric properties of mixed-phase, partially-melted precipitation particles are included in the simulations. Moreover, the FS, core-shell dielectric model for snow, combined with the MGwi dielectric model for graupel, produces the greatest overlap between the observed and simulated optical depth/reflectivity distributions. The observed distribution of melting layer optical depths includes some relatively large values that are not simulated by any of the melting models. These optical depths may be due to uncertainties in the observations and/or a lack of realism/generality in the melting simulations, including errors in the dielectric modeling of melting particles, precipitation particle size distributions which deviate from those observed, and a lack of robust stratiform regions overlying drier air which produce greater amounts of ice precipitation but less rainfall.

4. Summary and Outlook

In this study, a 1-D steady-state microphysical model which describes the vertical distribution of melting precipitation particles is developed. The model is driven by the ice-phase particle (snow, graupel) distributions just above the freezing level at applicable horizontal gridpoints of parent 3-D cloud-resolving model simulations, and extends these simulations by calculating the number density and meltwater fraction of each particle in finely-separated size categories through the melting layer. The depth of the modeled melting layer is primarily determined by the initial material density of ice-phase particles: distributions of constant-density snow (0.1 g cm^{-3}) and graupel (0.4 g cm^{-3}) generally melt over a deeper layer than distributions of snow and graupel having densities that decrease with particle size.

The radiative properties of melting precipitation at microwave frequencies are calculated based upon different methods for describing the dielectric properties of mixed-phase particles. Particle absorption and scattering efficiencies from 10.65 to 85.5 GHz are enhanced greatly for relatively small (~0.1) meltwater fractions. The relatively large numbers of these partially-melted particles just below the freezing level in stratiform regions lead to significant microwave absorption, exceeding the absorption by rain below the melting layer by factors of 10, 5, 3, and 2 at 10.65, 19.35, 37.0 and 85.5 GHz, respectively, in one test profile. Calculated backscatter efficiencies at 13.8 GHz increase in proportion to the particle meltwater fraction, leading to a "bright-band" of enhanced radar reflectivities in agreement with previous studies.

The radiative properties of melting layer are determined by the choice of dielectric models and the initial water contents and material densities of the ice-phase precipitation particles. In an attempt to resolve these sources of ambiguity in the melting layer model, four sets of melting profiles are generated based upon two tropical squall line CRM simulations. The control set contains no mixed phase precipitation, while the other sets include mixed-phase particles with radiative properties determined by different dielectric models and initial particle density distributions. The set of profiles based upon snow described by the Fabry-Szyrmer core-shell dielectric model and graupel described by the Maxwell-Garnett water matrix dielectric model, with constant material densities of 0.1 g cm-3 and 0.4 g cm-3, respectively, leads to reasonable consistency with PR-derived melting layer optical depth distributions. Snow and graupel with initial size-dependent densities produce a similar optical depth distribution if the same dielectric models are utilized. A more general conclusion from the intercomparison is that the control profiles which do not contain mixed-phase particles yield optical depths that are systematically lower than those observed. Therefore, the use of the melting layer model to extend 3-D

CRM simulations appears justified, at least until more realistic spectral methods for describing melting precipitation in 3-D CRM's are implemented.

Independent in situ measurements of particle size distributions in stratiform regions from airborne probe data have recently been performed as part of the TRMM field campaigns. Coupled with coincident airborne radiometer and radar observations, these data will hopfully lead to a more complete description of the microphysical and radiative properties of melting precipitation. A comparison of modeled and observed melting layer properties will be the focus of a future investigation by the authors of this study.

In Part II of this series, the 3-D CRM simulations listed in Table 1, augmented by the 1-D model in stratiform regions, serve as the basis for calculations of upwelling radiances at the TMI frequencies and computations of extinction/reflectivities at the PR frequency.

Acknowledgments

The authors would like to thank Brad Ferrier, Christian Kummerow, and Ye Hong for their helpful suggestions throughout the course of this study. Robert Meneghini and Liang Liao provided their invaluable expertise on the implementation of the radar "mirror image" technique. The research effort was supported by the TRMM Science program.

References

Awaka, J., T. Iguchi, and K. Okamoto, 1998: Early results on rain type classification by the Tropical Rainfall Measuring Mission (TRMM) precipitation radar. Proc. 8th URSI Commission F Open Symp., Aveiro, Portugal, 143-146.

Bauer, P., J. P. V. Poiares Baptista, and M. Iulis, 1999a: On the effect of the melting layer on microwave emission of clouds over the ocean. *J. Atmos. Sci.*, **56**, 852-867.

Bauer, P., A. Khain, I. Sednev, R. Meneghini, C. Kummerow, F. Marzano, and J. P. V. Poaires Baptista, 1999b: Combined cloud-microwave radiative transfer modeling of stratiform rainfall. Submitted to *J. Atmos. Sci.*

Bohren, C. F., and L. J. Battan, 1982: Radar backscattering of microwaves by spongy ice spheres. *J. Atmos. Sci.*, **39**, 2623-2629.

Bohren, C. F., and D. R. Huffman, 1983: *Absorption and Scattering of Light by Small Particles.* Wiley Press, 530 pp.

Bruggeman, D. A. G, 1935: Berechnung verschiedener physikalischer Konstanten von heterogenen Substanzen. *Ann. Phys. (Liepzig)*, **24**, 636-679.

Debye, P., 1929: *Polar Molecules, the Chemical Catalog Company*, 172 pp.

Ebert, E. E., and M. J. Manton, 1998: Performance of satellite rainfall estimation algorithms during TOGA COARE. *J. Atmos. Sci.*, **55**, 1537-1557.

Ferrier, B., 1994: A double-moment multiple-phase four-class bulk ice scheme. Part I: Description. *J. Atmos. Sci.*, **51**, 249-280.

Flatau, P., G. J. Tripoli, J. Berlinder, and W. Cotton, 1989: The CSU-RAMS cloud microphysics model: General theory and code documentation. Atmospheric Sciences Report No. 451, Colorado State University, Fort Collins, CO, 88 pp.

Fabry, F., and W. Szyrmer, 1999: Modeling of the melting layer. Part II: Electromagnetics. Submitted to *J. Atmos. Sci.*

Haddad, Z. S., E. A. Smith, C. D. Kummerow, T. Iguchi, M. R. Farrar, S. L. Durden, M. Alves, and W. S. Olson, 1997: The TRMM 'Day-1' radar/radiometer combined rain-profiling algorithm. *J. Meteor. Soc. Japan*, **75**, 799-808.

Klaassen, W., 1988: Radar observations and simulation of the melting layer of precipitation. *J. Atmos. Sci.*, **45**, 3741-3753.

Kummerow, C., 1998: Beamfilling errors in passive microwave rainfall retrievals. *J. Appl. Meteor.*, **37**, 356-370.

Liao, L., R. Meneghini, and T. Iguchi, 1999: Simulations of mirror image returns of air/space-borne radars in rain and their applications in estimating path attenuation. *IEEE Trans. on Geosci. Remote Sensing*, **37**, 1107-1121.

Lin, Y.-L., R. D. Farley, and H. D. Orville, 1983: Bulk parameterization of the snow field in a cloud model. *J. Climate Appl. Meteor.*, **22**, 1065-1092.

Locatelli, J. D., and P. V. Hobbs, 1974: Fall speeds and masses of solid precipitation particles. *J. Geophys. Res.*, **79**, 2185-2197.

Maxwell-Garnett, J. C., 1904: Colors in metal glasses and in metallic films. *Philos. Trans. Roy. Soc. London Ser. A*, **203**, 385-420.

Meneghini, R., and L. Liao, 1996: Comparisons for cross sections for melting hydrometeors as derived from dielectric mixing formulas and a numerical method. *J. Appl. Meteor.,* **35**, 1658-1670.

Meneghini, R., and L. Liao, 1997: Effective dielectric constants of mixed-phase hydrometeors. Submitted to *J. Ocean. Atmos. Tech.*

Meneghini, R., T. Iguchi, T. Kozu, L. Liao, K. Okamoto, J. A. Jones, J. Kwiatkowski, 1999: Use of the surface reference technique of path attenuation estimates from TRMM radar. Submitted to *J. Appl. Meteor.*

Mitchell, D. L., R. Zhang, and R. L. Petter, 1990: Mass-dimensional relationships for ice particles and the influence of riming on snowfall rates. *J. Appl. Meteor.*, **29**, 153-163.

Mugnai, A., H. J. Cooper, E. A. Smith, and G. J. Tripoli, 1990: Simulation of microwave brightness temperatures of an evolving hailstorm at SSM/I frequencies. *Bull. Amer. Meteor. Soc.*, **71**, 2-13.

Panegrossi, G., S. Dietrich, F. S. Marzano, A. Mugnai, E. A. Smith, X. Xiang, G. J. Tripoli, P. K. Wang, and J. P. V. Poiares Baptista, 1998: Use of cloud model microphysics for passive microwave-based precipitation retrieval: Significance of consistency between model and measurement manifolds. *J. Atmos. Sci.*, **55**, 1644-1673.

Pruppacher, H. R., and J. D. Klett, 1978: *Microphysics of Clouds and Precipitation.* Reidel, 714 pp.

Rutledge, S. A., and P. V. Hobbs, 1983: The mesoscale and microscale structure and organization of clouds and precipitation in midlatitude cyclones. Part VIII: A model for the "seeder-feeder" process in warm-frontal rainbands. *J. Atmos. Sci.*, **40**, 1185-1206.

Rutledge, S. A., and P. V. Hobbs, 1984: The mesoscale and microscale structure and organization of clouds and precipitation in midlatitude cyclones. XII: A diagnostic modeling study of precipitation development in narrow cold-frontal rainbands. *J. Atmos. Sci.*, **41**, 2949-2972.

Schols, J., J. Haferman, J. Weinman, C. Prabhakara, M. Cadeddu, and C. Kummerow, 1997: Polarized microwave radiation model of melting deformed hydrometeors. Preprints, *Ninth Conf. on Atmospheric Radiation*, Long Beach, CA, Amer. Meteor. Soc., 270-273.

Shivola, A., and I. V. Lindell, 1989: Polarizability and effective permittivity of layered and continuously inhomogeneous dielectric spheres. *J. Electrom. Waves Appl.*, **3**, 37-60.

Smith, E. A., C. D. Kummerow, and A. Mugnai, 1994: The emergence of inversion-type precipitation profile algorithms for estimation of precipitation from satellite microwave measurements. *Remote Sens. Rev.*, **11**, 211-242.

Szyrmer, W. and I. Zawadski, 1999: Modeling of the melting layer. Part I: Dynamics and microphysics. *J. Atmos. Sci.*, in press.

Tao, W.-K., and J. Simpson, 1993: Goddard Cumulus Ensemble Model. Part I: Model description. *Terrest. Atmos. Oceanic Sci.*, **4**, 35-72.

Tripoli, G. J., 1992a: A nonhydrostatic model designed to simulate scale interaction. *Mon. Wea. Rev.*, **120**, 1342-1359.

Tripoli, G. J., 1992b: An explicit three-dimensional nonhydrostatic numerical simulation of a tropical cyclone. *Meteor. Atmos. Phys.*, **49**, 229-254.

Tables

Table 1. Characteristics of the parent 3-D cloud-resolving model simulations.

Model/Simulation	Date	Approx. Location	Horizontal Resolution [km]	Grid Dimensions	Duration
GCE/TOGA1	2/22/93	9S, 159E	1 x 1	128 x 128 x 30	6 hours
GCE/TOGA3	2/22/93	9S, 159E	3 x 3	128 x 128 x 30	6 hours
GCE/TOGA2	12/19/92	2S, 155E	2 x 2	256 x 256 x 40	7 days
UW-NMS/ COHMEX	7/11/96	35N, 87W	1 x 1	51 x 51 x 42	4 hours
UW-NMS/ HURRICANE	9/11/88	19N, 70W	3.3 x 3.3[†]	62 x 62 x 42[†]	6 hours[†]

[†] refers to highest-resolution nested grid

Figure Captions

Fig. 1. Schematic of the grid domain of the 1-D melting layer model.

Fig. 2. Plan view of the surface rainfall rate distribution at 180 min from the TOGA1 CRM simulation. The location of the test profile is indicated by the cross-hairs.

Fig. 3. Melting layer model vertical profiles of (a) precipitation water contents, and (b) precipitation mass fluxes based upon melting of snow and graupel with size-independent densities. Panels (c) and (d) are the same as (a) and (b), but for snow and graupel densities that decrease with size.

Fig. 4. The real and imaginary parts of the refractive indices of melting snow based upon different dielectric constant models at (a) 10.65 GHz, (b) 19.35 GHz, (c) 37 GHz, and (d) 85.5 GHz. The lower-left vertex of the model curves in each panel represents dry snow, while the upper-right vertex represents completely melted snow. The "+" on each model curve represents a melted particle fraction of 0.5 by volume.

Fig. 5. Same as Fig. 4 but for melting graupel.

Fig. 6. Absorption and scattering efficiencies at 10.65 GHz (a and b), 19.35 GHz (c and d), 37.0 GHz (e and f), and 85.5 GHz (g and h), plotted as functions of particle radius based upon the Fabry-Szyrmer core-shell dielectric constant model for snow particles with meltwater volume fractions of 0.0, 0.01, 0.1, 0.4, and 1.0.

Fig. 7. Melting layer vertical profiles of (a) absorption coefficient, and (b) scattering coefficient at 10.65, 19.35, 37.0, and 85.5 GHz, based upon the Fabry-Szyrmer core-shell dielectric constant model applied to the snow and graupel distributions plotted in Fig. 3a. Absorption coefficient and scattering coefficient profiles in panels (c) and (d) are based upon the Maxwell-Garnett water matrix dielectric constant model.

Fig. 8. Extinction and backscatter efficiencies at 13.8 GHz, plotted as functions of particle radius based upon the Fabry-Szyrmer core-shell dielectric constant model for snow particles with meltwater volume fractions of 0.0, 0.01, 0.1, 0.4, and 1.0.

Fig. 9. Melting layer vertical profiles of (a) extinction, and (b) reflectivity at 13.8 GHz, based upon the Fabry-Szyrmer core-shell dielectric constant model applied to the snow and graupel distributions plotted in Fig. 3a. Extinction and reflectivity profiles in panels (c) and (d) are based upon the Maxwell-Garnett water matrix dielectric constant model.

Fig. 10. Melting layer vertical profiles of (a) extinction, and (b) reflectivity at 13.8 GHz, based upon the Fabry-Szyrmer core-shell dielectric constant model applied to the snow and graupel distributions plotted in Fig. 3c.

Fig. 11. Schematic of reference levels utilized to determine melting layer extinction optical depths from measurements of the Precipitation Radar.

Fig. 12. Extinction optical depths of simulated melting layers (black dots), plotted as functions of attenuation-corrected basal reflectivities, using (a) no mixed-phase particles, (b) Fabry-Szyrmer core-shell model snow and Maxwell-Garnett water matrix model graupel, (c) Fabry-Szyrmer core-shell model snow and Meneghini-Liou 1997 model graupel, and (d) Fabry-Szyrmer core-shell model snow and Maxwell-Garnett water-matrix model graupel (but for snow and graupel densities that decrease with particle size). Melting layers are derived from the TOGA1 and TOGA3 cloud-resolving model simulations; ref. Table 1. Also, observed melting layer extinction optical depths (diamonds) are plotted as functions of attenuation-corrected basal reflectivities. Observed optical depths are estimated using the mirror-image technique, applied to observations of the Precipitation Radar at low latitiudes. Representative error bars are indicated for one pair of observations.

Fig. 1

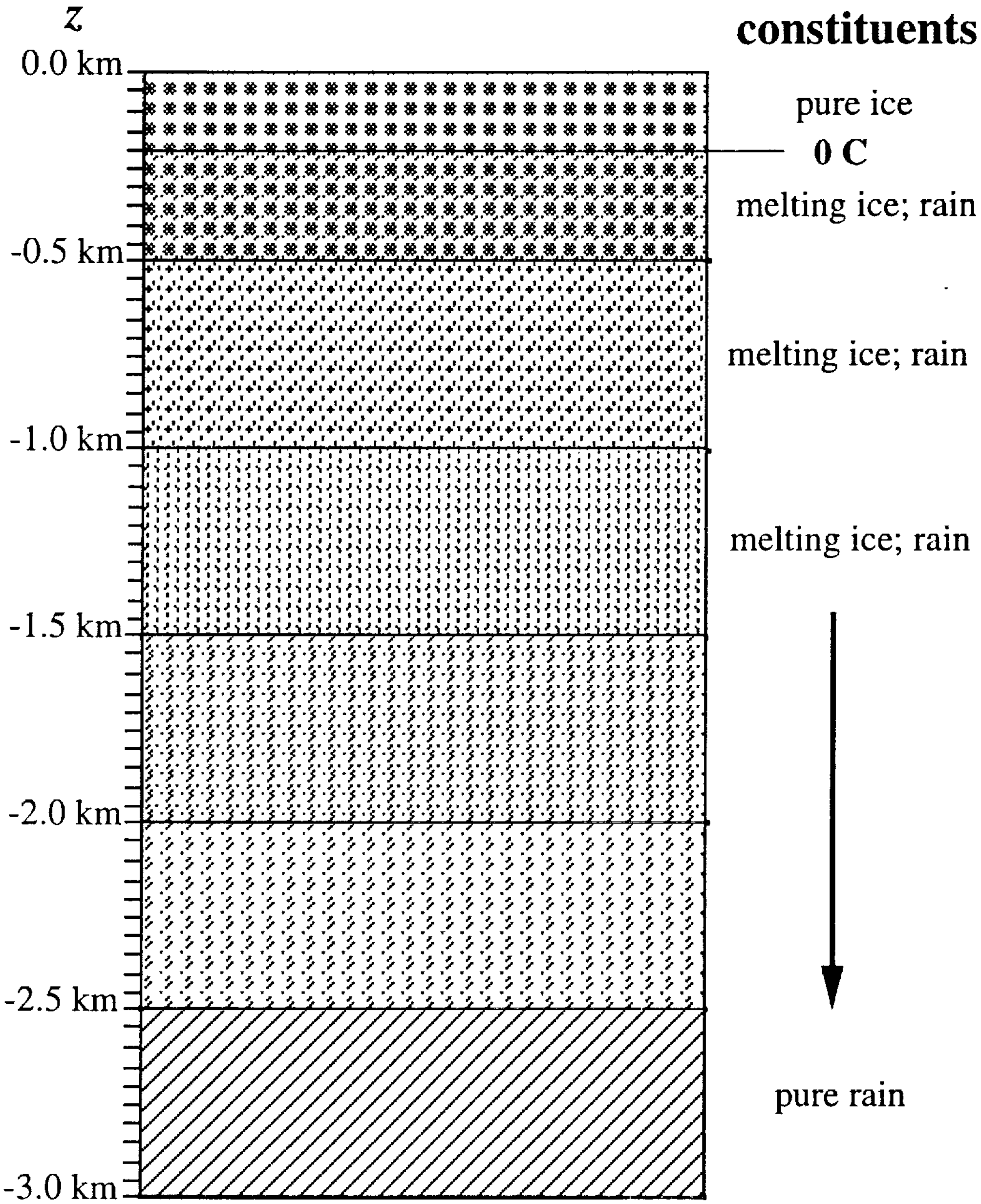
z
constituents
0.0 km
pure ice
0 C
melting ice; rain
-0.5 km
melting ice; rain
-1.0 km
melting ice; rain
-1.5 km
-2.0 km
-2.5 km
pure rain
-3.0 km

Fig. 2

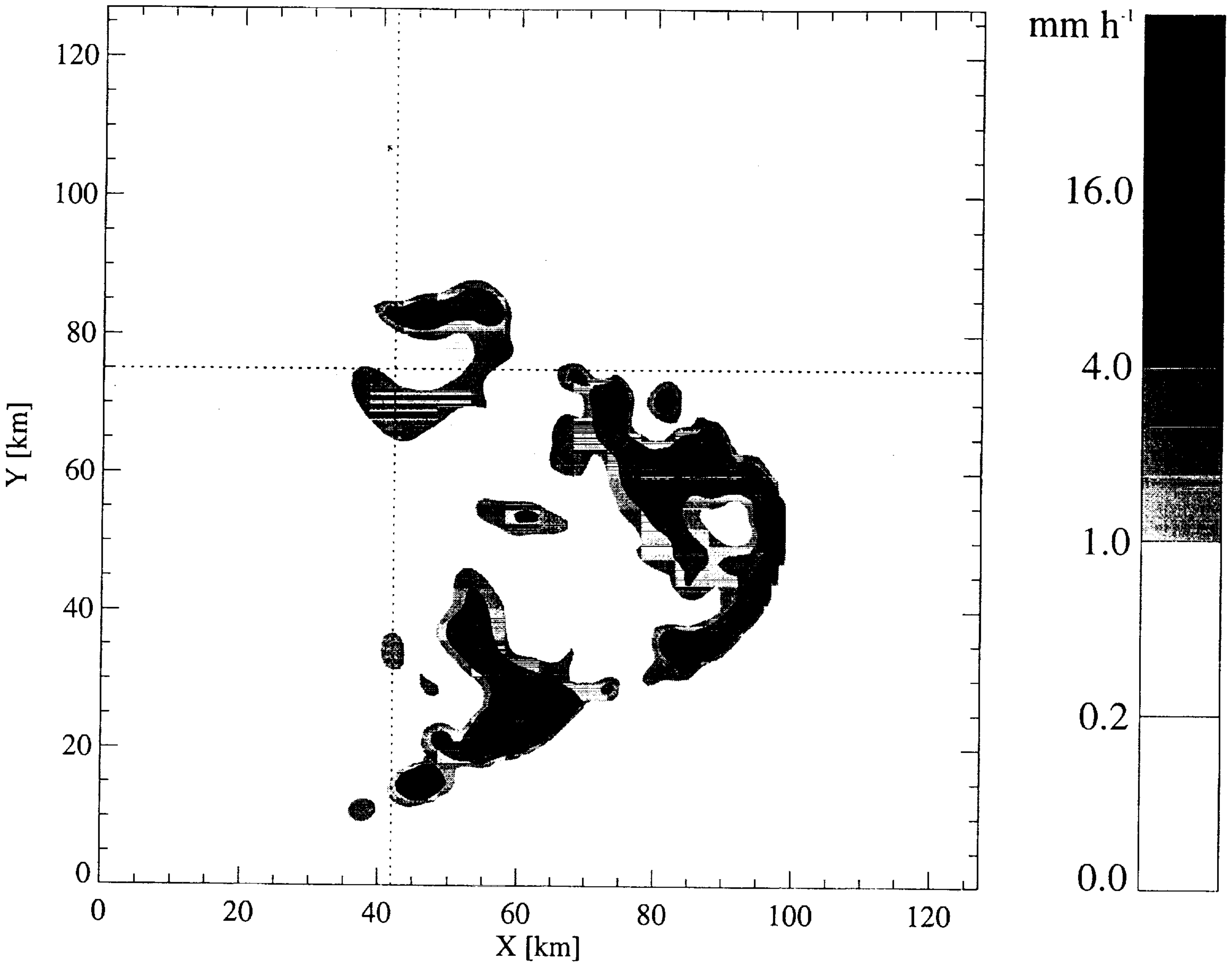

120
100
80
60
40
20
0
Y [km]
0
20
40
60
80
100
120
X [km]
mm h⁻¹
16.0
4.0
1.0
0.2
0.0

Fig. 3

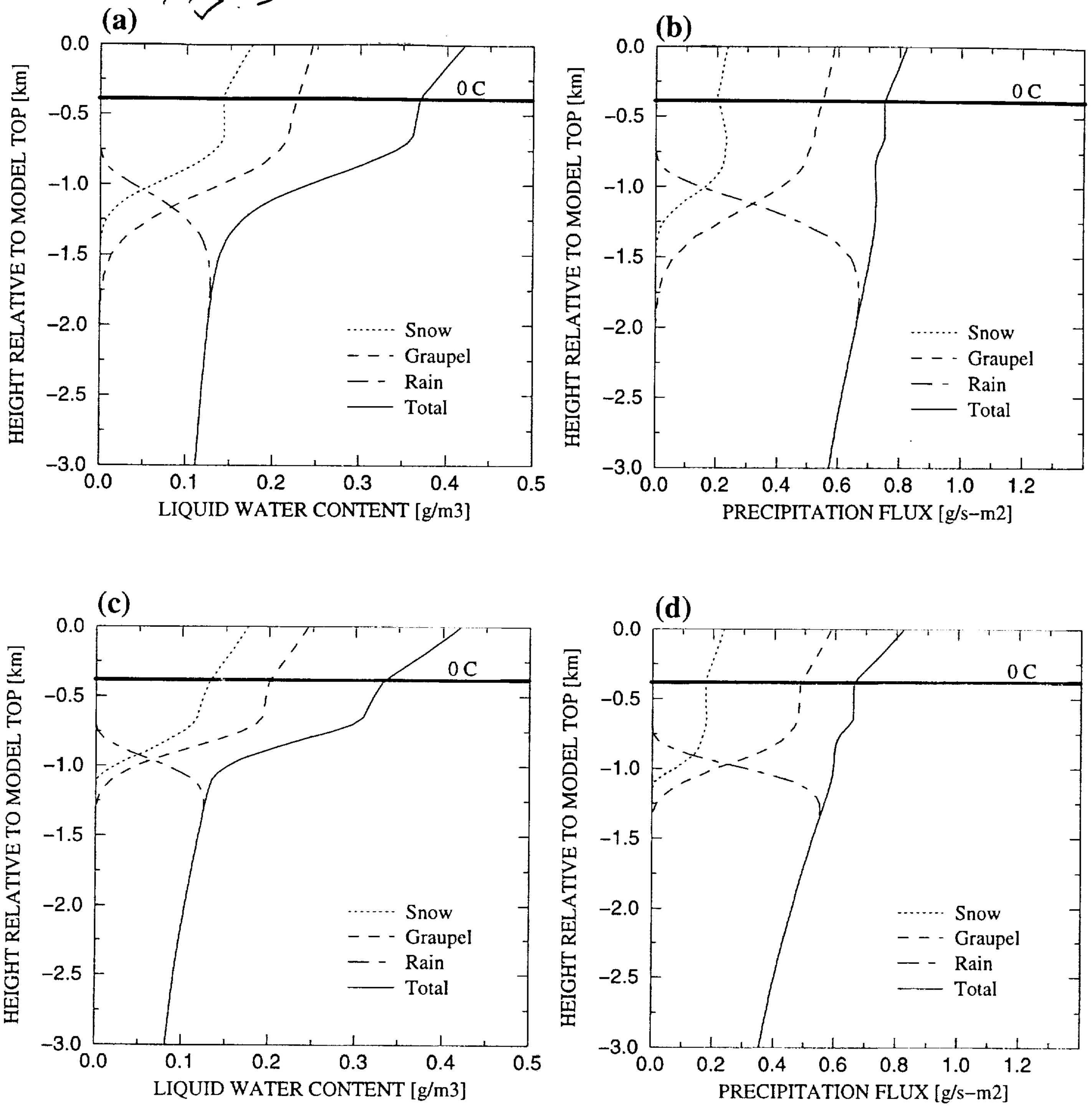
(a)
HEIGHT RELATIVE TO MODEL TOP [km]
0.0
-0.5
-1.0
-1.5
-2.0
-2.5
-3.0
0 C
Snow
Graupel
Rain
Total
0.0
0.1
0.2
0.3
0.4
0.5
LIQUID WATER CONTENT [g/m3]
(b)
HEIGHT RELATIVE TO MODEL TOP [km]
0 C
Snow
Graupel
Rain
Total
0.0
0.2
0.4
0.6
0.8
1.0
1.2
PRECIPITATION FLUX [g/s-m2]
(c)
HEIGHT RELATIVE TO MODEL TOP [km]
0 C
Snow
Graupel
Rain
Total
LIQUID WATER CONTENT [g/m3]
(d)
HEIGHT RELATIVE TO MODEL TOP [km]
0 C
Snow
Graupel
Rain
Total
PRECIPITATION FLUX [g/s-m2]

Fig.4

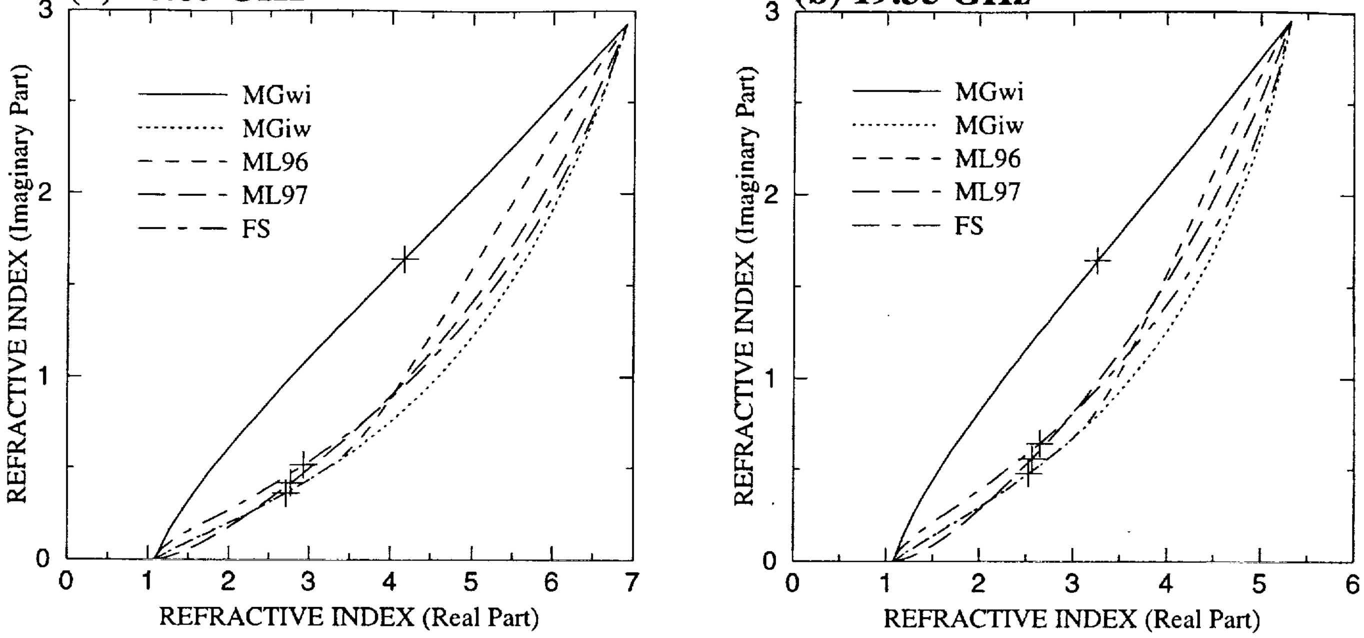
(a) 10.65 GHz

(b) 19.35 GHz

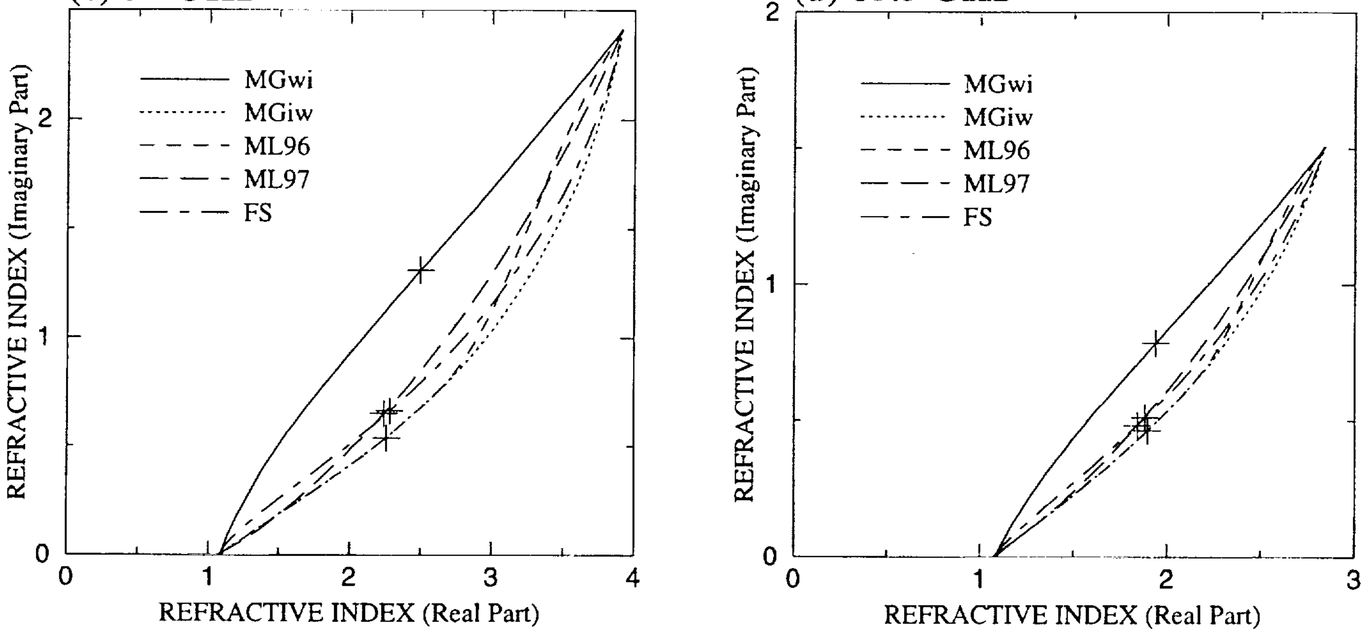
(c) 37 GHz

(d) 85.5 GHz

Fig. 5

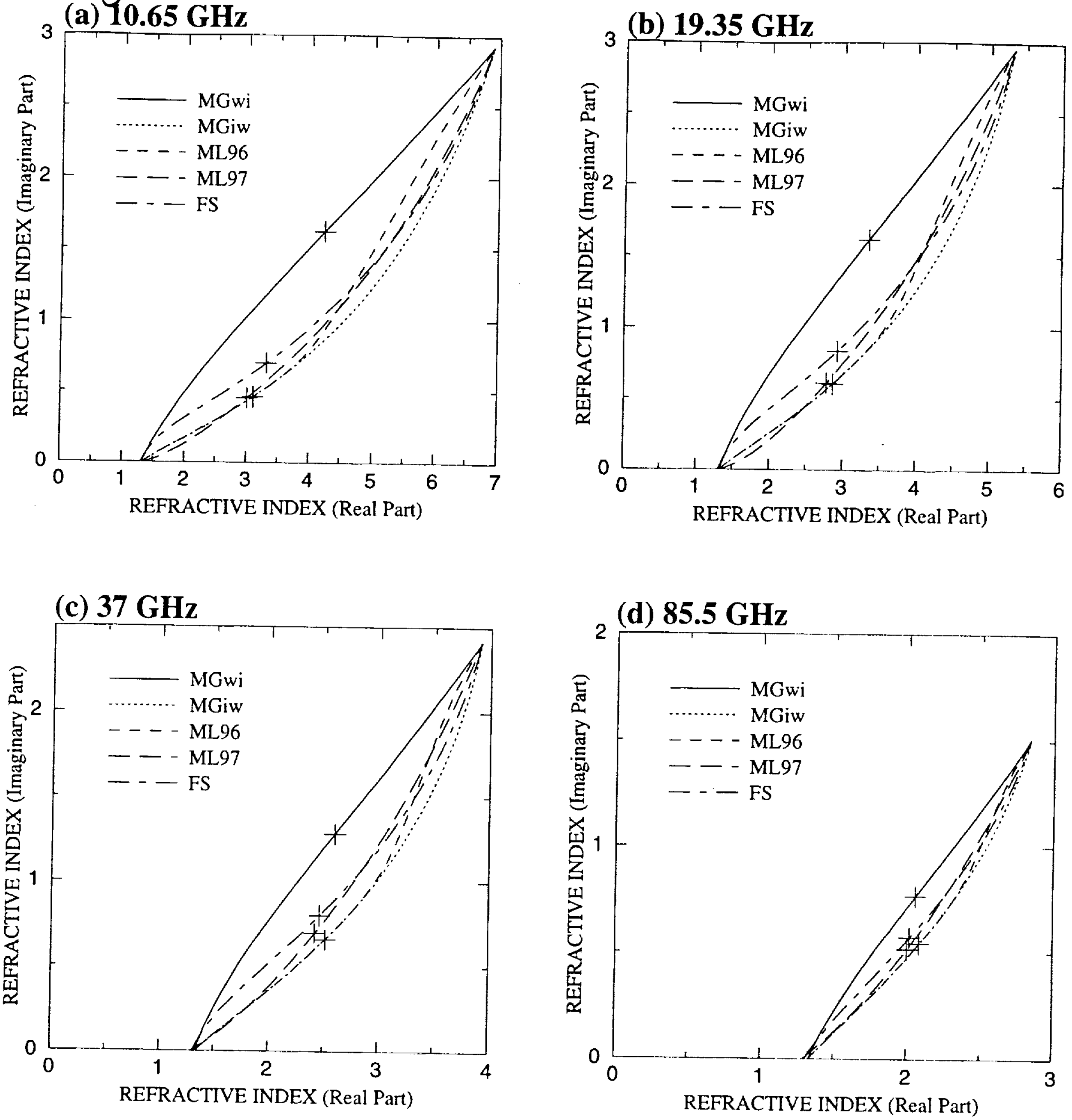
(a) 10.65 GHz

(b) 19.35 GHz

(c) 37 GHz

(d) 85.5 GHz

Fig. 6

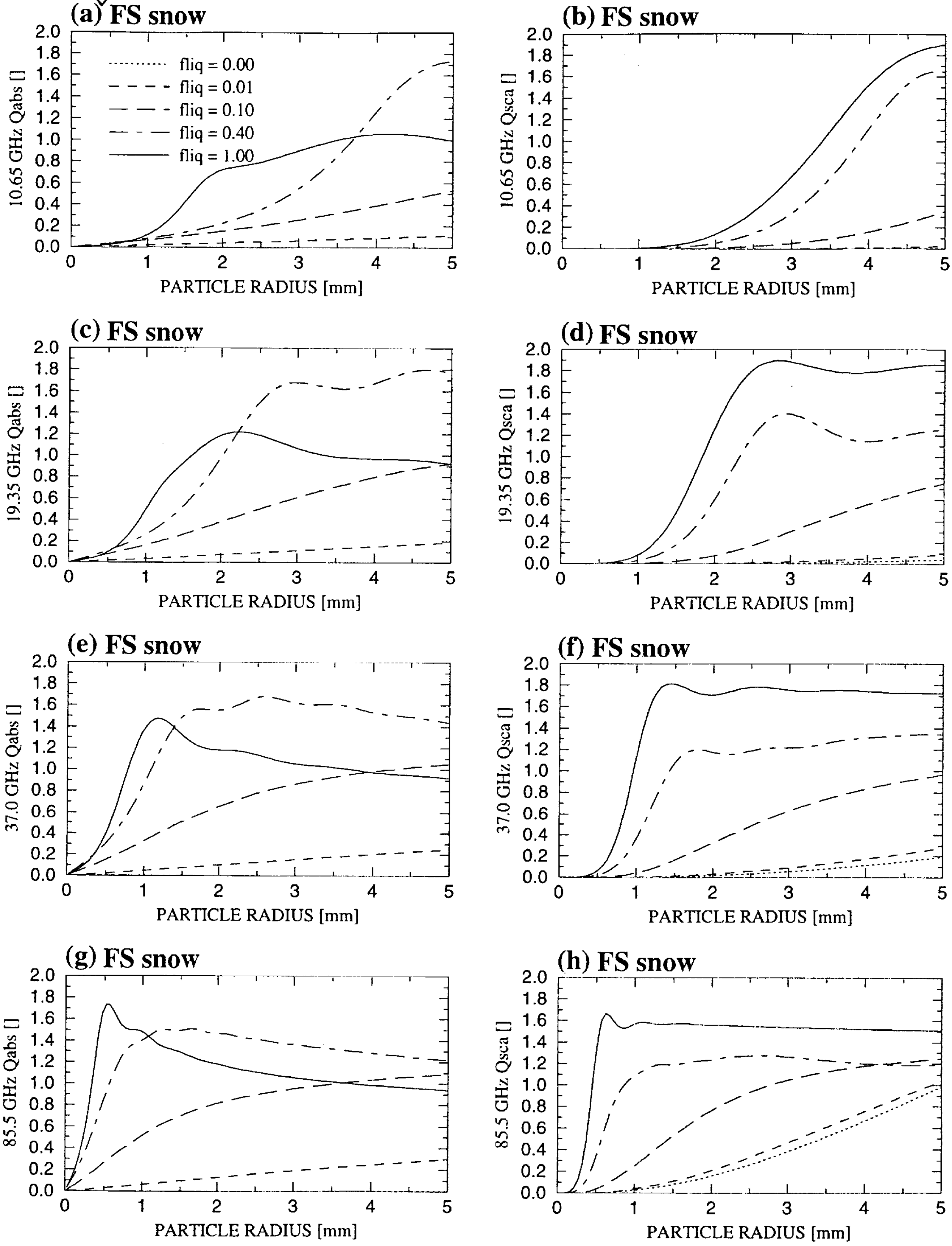
(a) FS snow
10.65 GHz Qabs []
fliq = 0.00
fliq = 0.01
fliq = 0.10
fliq = 0.40
fliq = 1.00
(b) FS snow
10.65 GHz Qsca []
(c) FS snow
19.35 GHz Qabs []
(d) FS snow
19.35 GHz Qsca []
(e) FS snow
37.0 GHz Qabs []
(f) FS snow
37.0 GHz Qsca []
(g) FS snow
85.5 GHz Qabs []
(h) FS snow
85.5 GHz Qsca []
PARTICLE RADIUS [mm]
0.0
0.2
0.4
0.6
0.8
1.0
1.2
1.4
1.6
1.8
2.0
0
1
2
3
4
5

Fig. 7

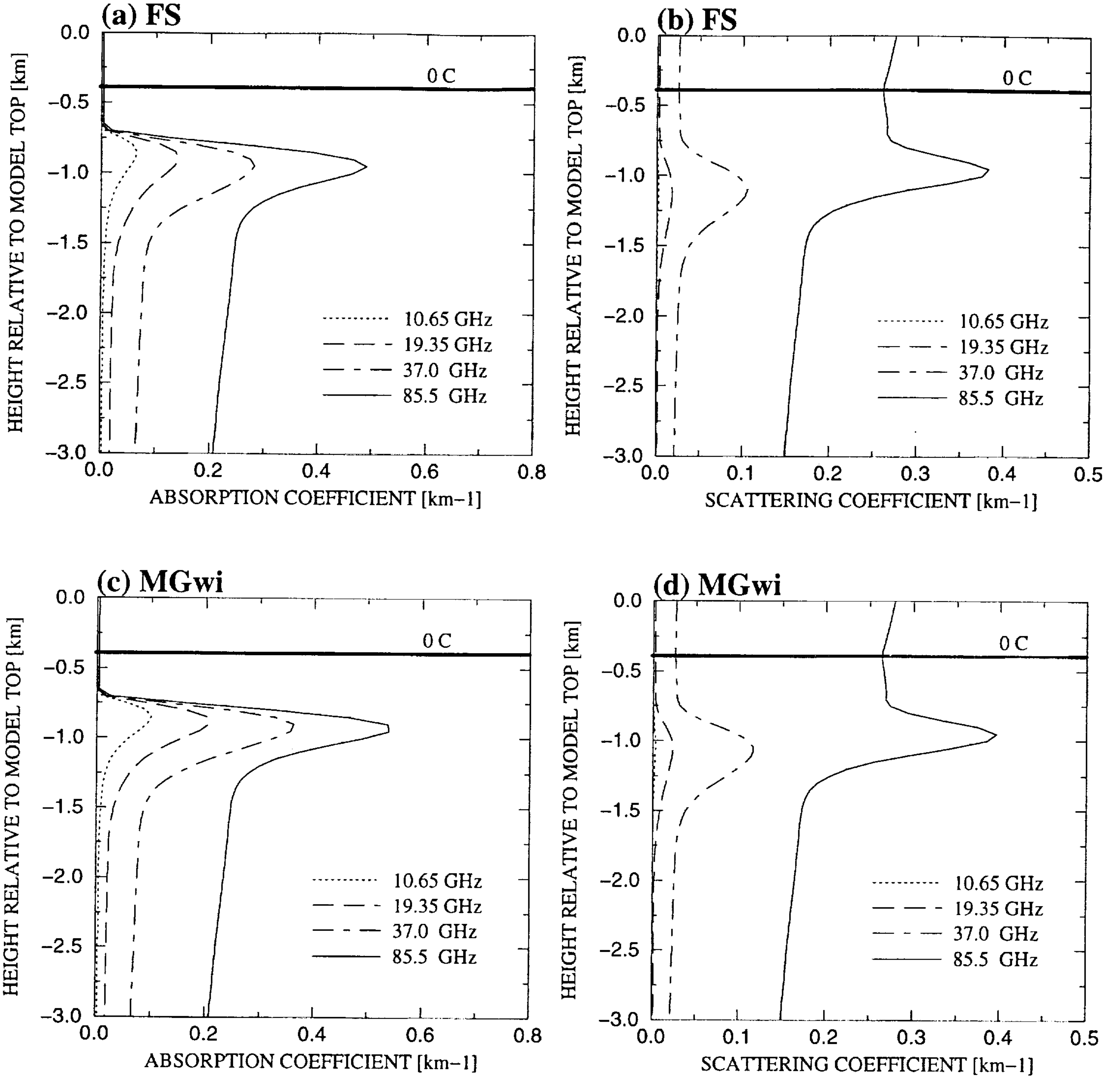
(a) FS
HEIGHT RELATIVE TO MODEL TOP [km]
0.0
-0.5
-1.0
-1.5
-2.0
-2.5
-3.0
0 C
10.65 GHz
19.35 GHz
37.0 GHz
85.5 GHz
0.0
0.2
0.4
0.6
0.8
ABSORPTION COEFFICIENT [km-1]
(b) FS
HEIGHT RELATIVE TO MODEL TOP [km]
0 C
10.65 GHz
19.35 GHz
37.0 GHz
85.5 GHz
0.0
0.1
0.2
0.3
0.4
0.5
SCATTERING COEFFICIENT [km-1]
(c) MGwi
HEIGHT RELATIVE TO MODEL TOP [km]
0 C
10.65 GHz
19.35 GHz
37.0 GHz
85.5 GHz
ABSORPTION COEFFICIENT [km-1]
(d) MGwi
HEIGHT RELATIVE TO MODEL TOP [km]
0 C
10.65 GHz
19.35 GHz
37.0 GHz
85.5 GHz
SCATTERING COEFFICIENT [km-1]

Fig. 8

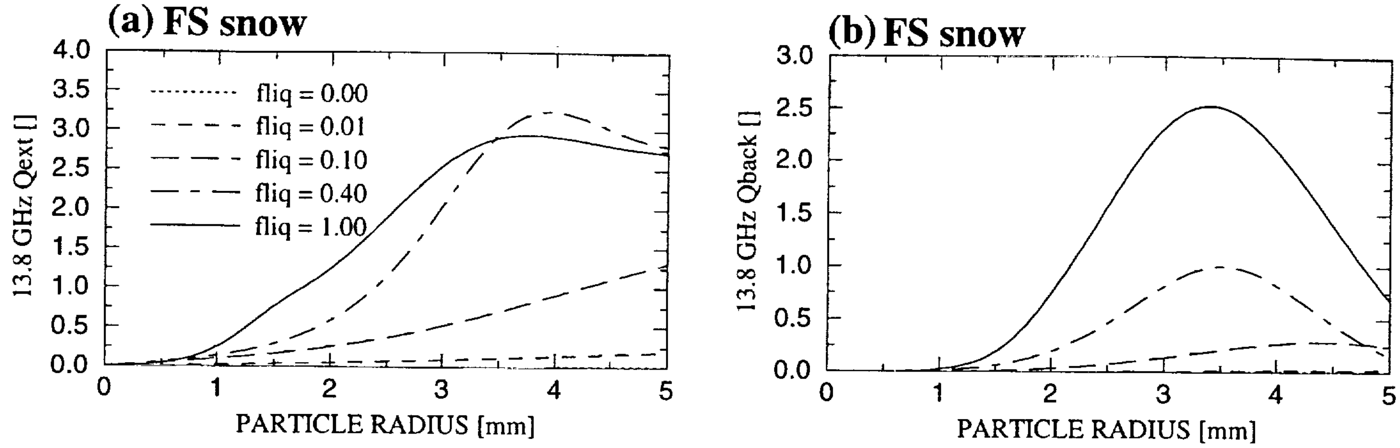
(a) FS snow
13.8 GHz Qext []
4.0
3.5
3.0
2.5
2.0
1.5
1.0
0.5
0.0
0
1
2
3
4
5
PARTICLE RADIUS [mm]
fliq = 0.00
fliq = 0.01
fliq = 0.10
fliq = 0.40
fliq = 1.00
(b) FS snow
13.8 GHz Qback []
3.0
2.5
2.0
1.5
1.0
0.5
0.0
0
1
2
3
4
5
PARTICLE RADIUS [mm]

Fig. 9

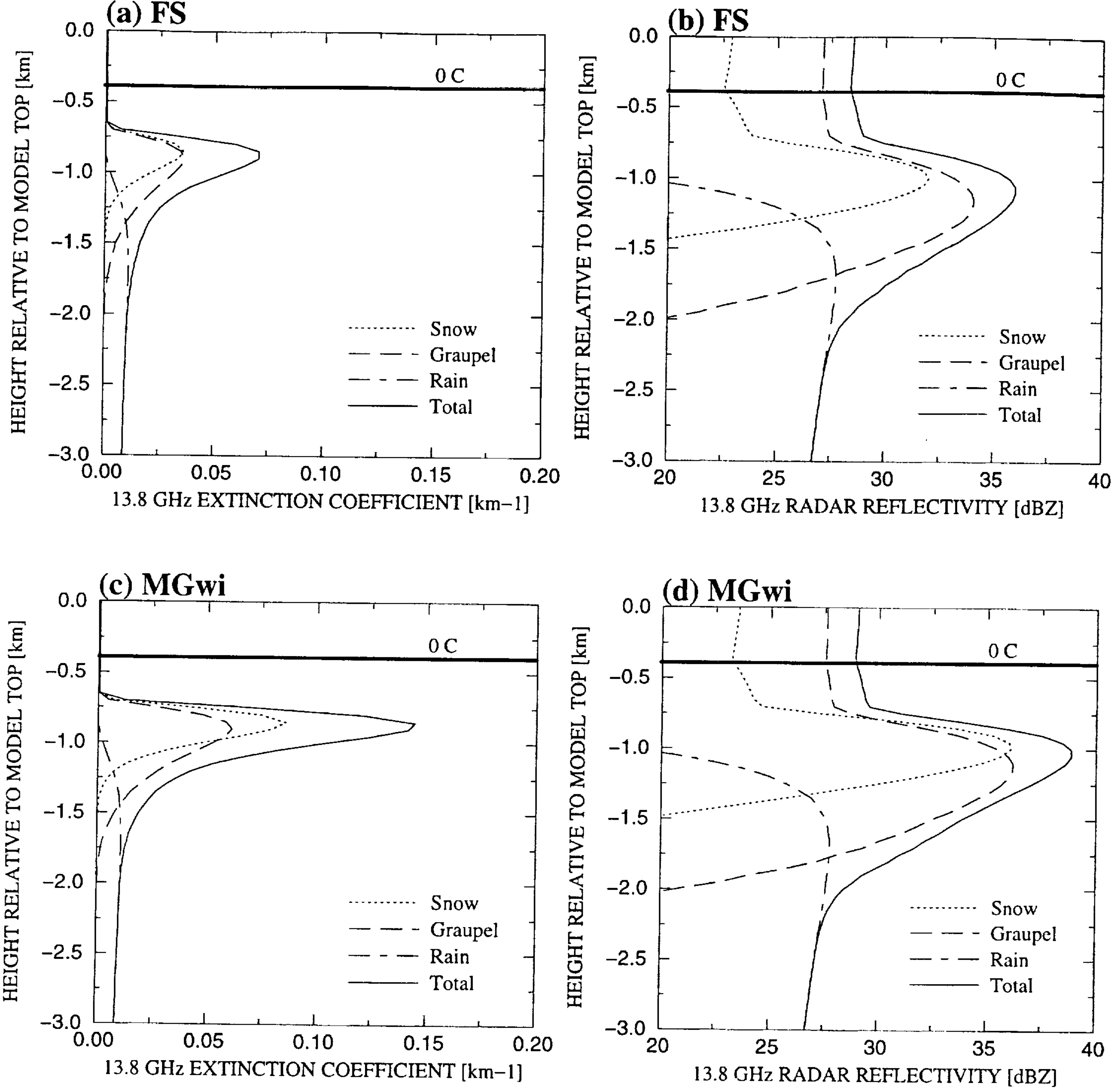
(a) FS
(b) FS
(c) MGwi
(d) MGwi
0 C
HEIGHT RELATIVE TO MODEL TOP [km]
0.0
-0.5
-1.0
-1.5
-2.0
-2.5
-3.0
13.8 GHz EXTINCTION COEFFICIENT [km-1]
0.00
0.05
0.10
0.15
0.20
13.8 GHz RADAR REFLECTIVITY [dBZ]
20
25
30
35
40
Snow
Graupel
Rain
Total

Fig. 10

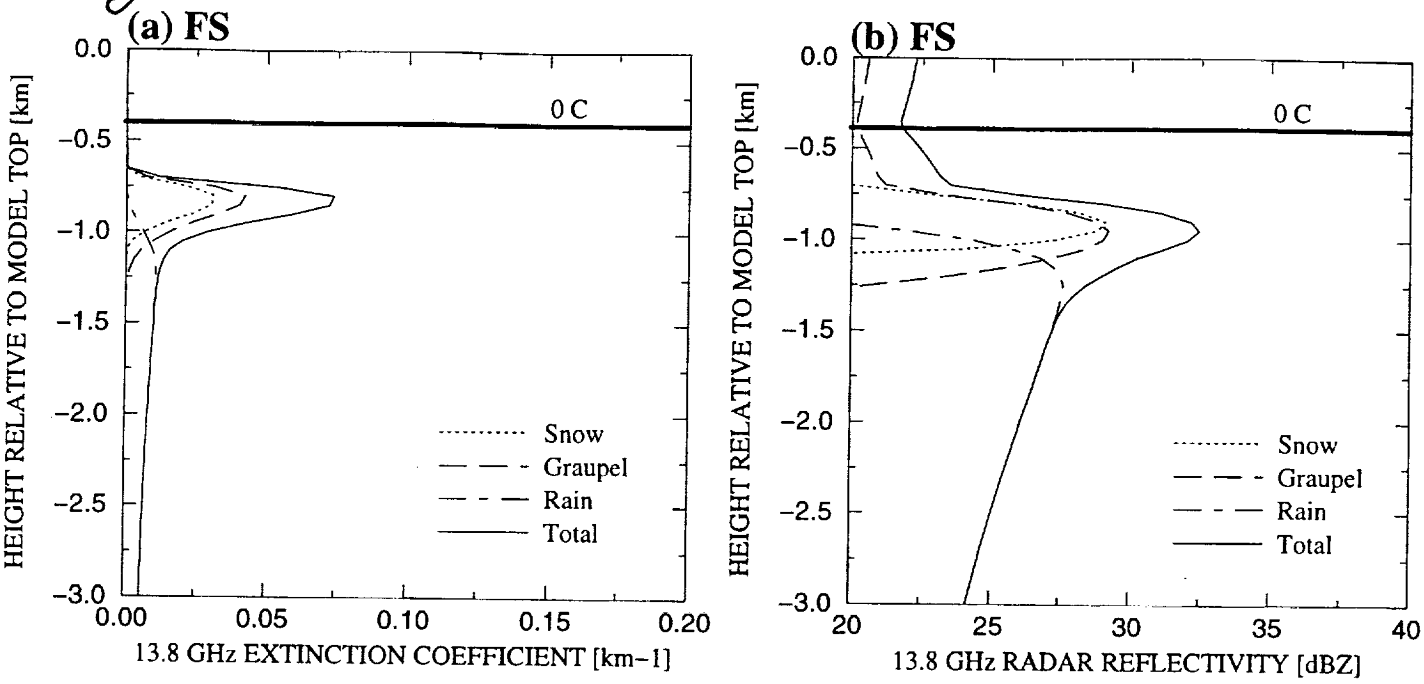
(a) FS
0.0
-0.5
-1.0
-1.5
-2.0
-2.5
-3.0
HEIGHT RELATIVE TO MODEL TOP [km]
0 C
Snow
Graupel
Rain
Total
0.00
0.05
0.10
0.15
0.20
13.8 GHz EXTINCTION COEFFICIENT [km-1]
(b) FS
0.0
-0.5
-1.0
-1.5
-2.0
-2.5
-3.0
HEIGHT RELATIVE TO MODEL TOP [km]
0 C
Snow
Graupel
Rain
Total
20
25
30
35
40
13.8 GHz RADAR REFLECTIVITY [dBZ]

Fig. 11

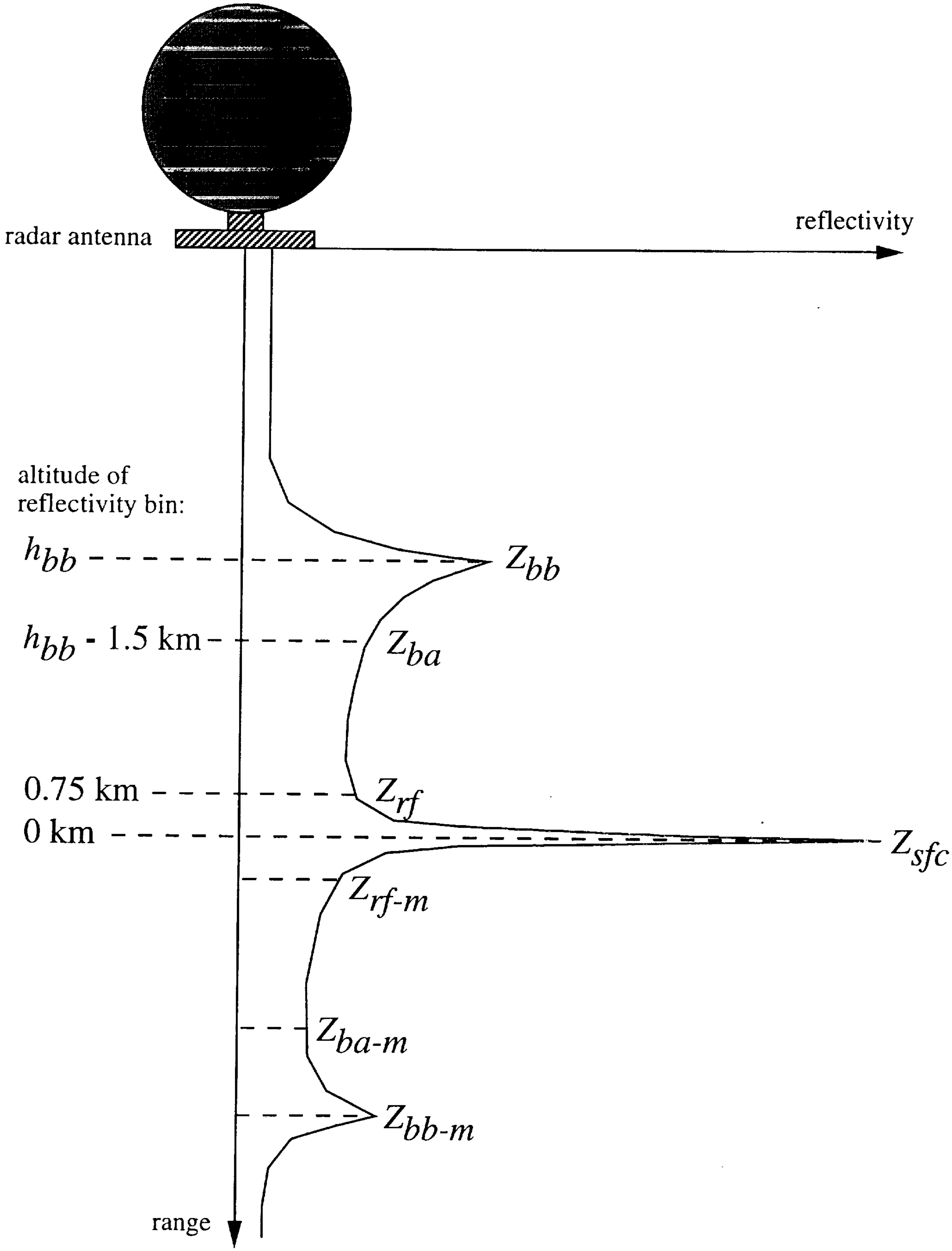

radar antenna
reflectivity
altitude of reflectivity bin:
h_{bb}
Z_{bb}
h_{bb} - 1.5 km
Z_{ba}
0.75 km
Z_{rf}
0 km
Z_{sfc}
$Z_{rf\text{-}m}$
$Z_{ba\text{-}m}$
$Z_{bb\text{-}m}$
range

Fig.12

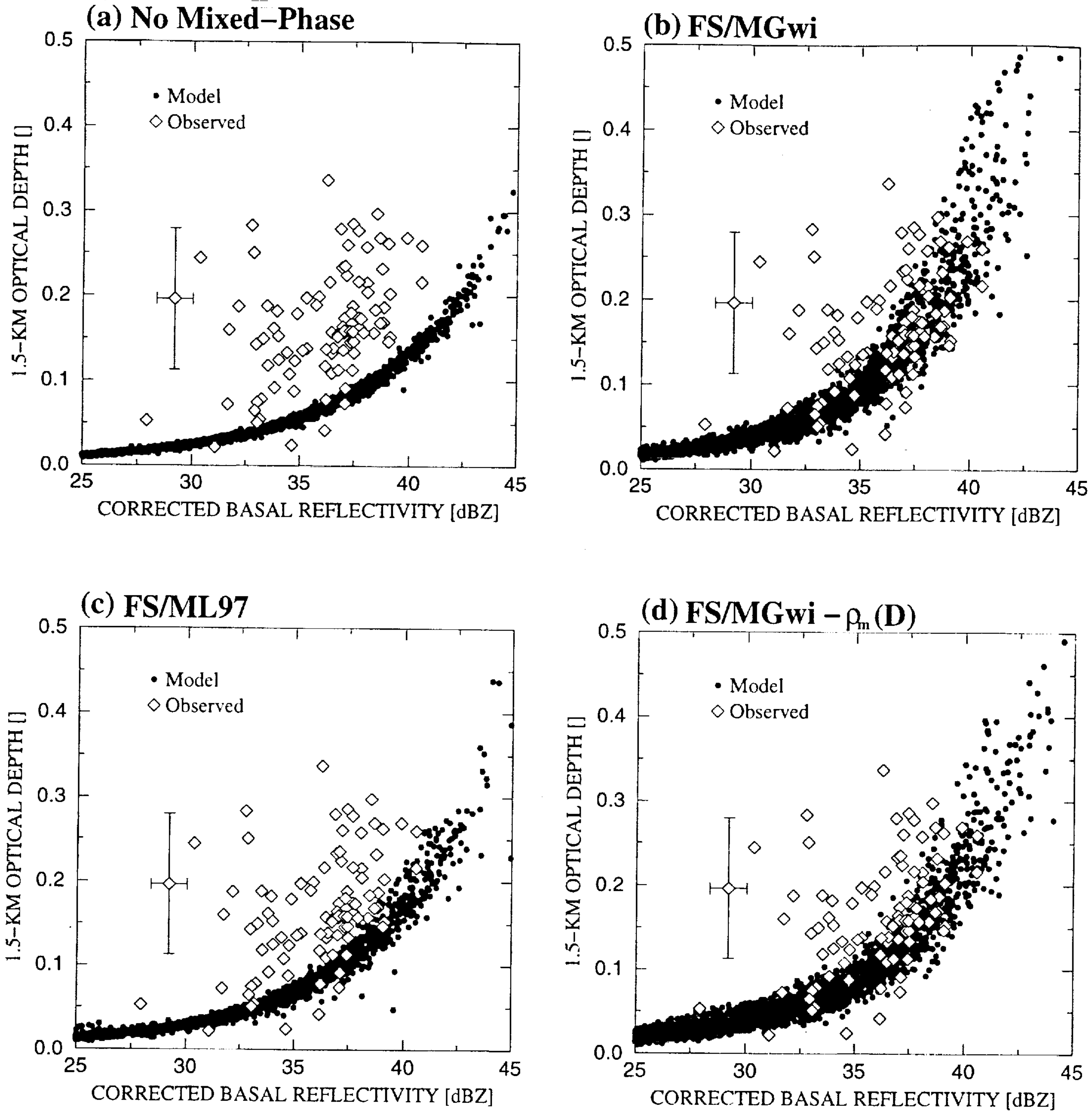
(a) No Mixed-Phase

(b) FS/MGwi

(c) FS/ML97

(d) FS/MGwi – ρ_m(D)